DEVELOPMENT AND ADDITIVE MANUFACTURING OF REFRACTORY HIGH ENTROPY ALLOYS FOR EXTREME ENVIRONMENT APPLICATIONS

A THESIS SUBMITTED TO
THE GRADUATE SCHOOL OF NATURAL AND APPLIED SCIENCES
OF
MIDDLE EAST TECHNICAL UNIVERSITY

BY

ÖZGÜN UMUT TUKAÇ

IN PARTIAL FULFILLMENT OF THE REQUIREMENTS
FOR
THE DEGREE OF MASTER OF SCIENCE
IN
METALLURGICAL AND MATERIALS ENGINEERING

AUGUST 2023

Approval of the thesis:

DEVELOPMENT AND ADDITIVE MANUFACTURING OF REFRACTORY HIGH ENTROPY ALLOYS FOR EXTREME ENVIRONMENT APPLICATIONS

submitted by **ÖZGÜN UMUT TUKAÇ** in partial fulfillment of the requirements for the degree of **Master of Science** i**n Metallurgical and Materials Engineering, Middle East Technical University** by,

Prof. Dr. Halil Kalıpçılar
Dean, Graduate School of **Natural and Applied Sciences** _____

Prof. Dr. Ali Kalkanlı
Head of the Department, **Met. and Mat. Eng., METU** _____

Assist. Prof. Dr. Eda Aydoğan Güngör
Supervisor, **Met. and Mat. Eng., METU** _____

Examining Committee Members:

Prof. Dr. C. Hakan Gür
Metallurgical and Materials Eng, METU _____

Assist. Prof. Dr. Eda Aydoğan Güngör
Metallurgical and Materials Eng, METU _____

Prof. Dr. Arcan Dericioğlu
Metallurgical and Materials Eng, METU _____

Prof. Dr. Benat Koçkar
Mechanical Engineering, Hacettepe University _____

Assist. Prof. Dr. Irmak Sargın
Metallurgical and Materials Eng, METU _____

Date: 25.08.2023

I hereby declare that all information in this document has been obtained and presented in accordance with academic rules and ethical conduct. I also declare that, as required by these rules and conduct, I have fully cited and referenced all material and results that are not original to this work.

Name Last name : Özgün Umut Tukaç

Signature :

ABSTRACT

DEVELOPMENT AND ADDITIVE MANUFACTURING OF REFRACTORY HIGH ENTROPY ALLOYS FOR EXTREME ENVIRONMENT APPLICATIONS

Tukaç, Özgün Umut
Master of Science, Metallurgical and Materials Engineering
Supervisor: Assist. Prof. Dr. Eda Aydoğan Güngör

August 2023, 85 pages

This study primarily focuses on the development and manufacturing of Cr10Mo25Ta25Ti15V25 Refractory High Entropy Alloy (RHEA) using conventional and additive manufacturing (AM) techniques. The aim of this study was to develop a novel RHEA grade displaying attributes such as exceptional ductility, moderate density, and outstanding high-temperature stability. To design the alloy, a dual strategy of empirical calculations and CALPHAD (CALculation of PHAse Diagrams) studies was employed. First, conventional Vacuum Arc Melting (VAM) technique was used to produce a single phase Cr10Mo25Ta25Ti15V25 RHEA with small amount of FCC-Ti phase. This alloy, which showed no formation of the typically brittle HCP phase, exhibited impressive strength and ductility.

Directed Energy Deposition (DED) AM technique was explored for the Cr10Mo25Ta25Ti15V25 RHEA production. Detailed analyses highlighted challenges in achieving homogenization and identified distinct phase formations. More importantly, DED-produced RHEA samples displayed improved mechanical properties across different temperatures compared to VAM-produced samples.

Overall, this research emphasizes the potential and adaptability of the Cr10Mo25Ta25Ti15V25 RHEA for the varying production techniques, setting the foundation for further exploration and potential applications in the metallurgical industry.

Keywords: Refractory High Entropy Alloys, Additive Manufacturing, CALPHAD, Characterization, Mechanical Properties

ÖZ

AŞIRI ÇEVRE UYGULAMALARI İÇİN REFRAKTER YÜKSEK ENTROPİLİ ALAŞIMLARIN GELİŞTİRİLMESİ VE KATMANLI İMALATI

Tukaç, Özgün Umut
Yüksek Lisans, Metalurji ve Malzeme Mühendisliği
Tez Yöneticisi: Dr. Eda Aydoğan Güngör

Ağustos 2023, 85 sayfa

Bu çalışma, geleneksel ve eklemeli imalat (AM) teknikleri kullanılarak Cr10Mo25Ta25Ti15V25 Refrakter Yüksek Entropi Alaşımı (RYEA) geliştirmesi ve üretimine öncelikli olarak odaklanmaktadır. Bu çalışmanın amacı, olağanüstü süneklik, orta yoğunluk ve üstün yüksek sıcaklık kararlılığı gibi özellikleri gösteren yeni bir RYEA geliştirmektir. Alaşımın tasarımı için deneysel hesaplamaların ve CALPHAD (FAZ Diyagramlarının Hesaplanması) çalışmalarının çift yönlü bir stratejisi benimsenmiştir. İlk olarak, geleneksel Vakum Ark Eritme (VAM) tekniği kullanılarak küçük miktarda FCC-Ti fazıyla tek fazlı bir Cr10Mo25Ta25Ti15V25 RYEA üretildi. Tipik olarak kırılgan HCP fazının oluşumunu göstermeyen bu alaşım, etkileyici mukavemet ve süneklik sergiledi.

Yönlendirilmiş Enerji Depozisyonu (DED) AM tekniği, Cr10Mo25Ta25Ti15V25 RYEA üretimi için incelendi. Detaylı analizler, homojenizasyonun sağlanmasındaki zorlukları vurguladı ve belirgin faz oluşumlarını tanımladı. Daha da önemlisi, DED ile üretilen RYEA örnekleri, VAM ile üretilen örneklerle karşılaştırıldığında farklı sıcaklıklarda geliştirilmiş mekanik özellikler gösterdi.

Genel olarak, bu araştırma, Cr10Mo25Ta25Ti15V25 RYEA'nın çeşitli üretim teknikleri için potansiyelini ve uyarlanabilirliğini vurgulamakta ve metalürji endüstrisindeki daha fazla keşif ve potansiyel uygulamalar için temeli atmaktadır.

Anahtar Kelimeler: Refrakter Yüksek Entropili Alaşımlar, Eklemeli İmalat, CALPHAD, Karakterizasyon, Mekanik Özellikler

To my mother

ACKNOWLEDGMENTS

The author wishes to express his deepest gratitude to his supervisor Assist. Prof. Dr Eda Aydoğan for her guidance, advice, criticism, encouragements and insight throughout the research.

The author would also like to thank Prof. Dr. Arcan Dericioğlu, Prof. Dr. Bahattin Koç and Assist. Prof. Dr. Gökhan Polat for their suggestions and comments.

I would like to thank MATEXA-LAB members Merve Yeşim Yalçın, Ali Özalp, Berk Tanrısevdi, Hasan Tahsin Koç, Kadir Demirci, Aylin Aktaş and Yavuz Yıldız for their help and advice.

I would like to thank Materials Development Laboratory members Doğuhan Sarıtürk, Can Okuyucu and Fatma Saadet Güven for their help and advice.

This work is funded by Scientific and Technological Research Council of Turkey under grant number TUBİTAK 118C239.

TABLE OF CONTENTS

ABSTRACT v

ÖZ vii

ACKNOWLEDGMENTS x

TABLE OF CONTENTS xi

LIST OF TABLES xiv

LIST OF FIGURES xv

LIST OF ABBREVIATIONS xviii

LIST OF SYMBOLS xx

CHAPTERS

1 INTRODUCTION 1

2 LITERATURE REVIEW 3

2.1 High entropy alloys 3

2.1.1 Definition 4

2.1.2 Four core effect 5

2.1.3 Alloy design 7

2.2 Refractory high entropy alloys 12

2.2.1 Properties 13

2.3 Production methods of RHEAs 21

2.3.1 Vacuum Arc Melting 22

2.3.2 Mechanical alloying and material consolidation 23

2.3.3 Additive Manufacturing 25

3 METHODS AND EXPERIMENTAL PROCEDURE 31

3.1 Alloy design 31

3.1.1 Empirical calculations 31
3.1.2 CALPHAD 32
3.2 Production methods 33
3.2.1 Vacuum Arc Melter 33
3.2.2 Directed Energy Deposition 33
3.3 Characterization methods 35
3.3.1 X-Ray Diffraction 35
3.3.2 Microstructure Analysis with Optical Microscopy 36
3.3.3 Microstructure Analysis with Scanning Electron Microscopy 36
3.3.4 EBSD Analysis 36
3.3.5 TEM Analysis 37
3.4 Compression tests 37
3.4.1 Sample preparation 37
3.4.2 Test setup 38
3.4.3 Test parameters 38
4 RESULTS AND DISCUSSION 39
4.1 Alloy Design 39
4.2 Characterization of VAM samples 40
4.2.1 Microstructure 40
4.2.2 Phase analysis 40
4.3 Characterization of DED samples 42
4.3.1 Parameter optimization 42
4.3.2 Phase analysis 49
4.3.3 Microstructure 50

4.4 Effect of production method on Cr10Mo25Ta25Ti15V25 RHEA 51
4.4.1 EDX analysis 51
4.4.2 EBSD analysis 54
4.4.3 TEM analysis 57
4.4.4 Compression tests 62
5 CONCLUSION 67
REFERENCES 71

LIST OF TABLES

TABLES

Table 2.1 Empirical calculation criteria. 10
Table 2.2 Oxidation behavior of refractory elements. 18
Table 3.1 Production parameters used for first batch. 34
Table 3.2 Production parameters used for second batch. 35
Table 3.3 Compression test sample dimensions. 38
Table 4.1 The calculated thermophysical properties of Cr10Mo25Ta25Ti15V25 alloy. 39
Table 4.2 EDX analysis of sample 10. 48
Table 4.3 Pore analysis of samples 12, 13, and 14. 49

LIST OF FIGURES

FIGURES

Figure 2.1. Schematic representation of severe lattice distortion in BCC alloy[20]. ... 6
Figure 2.2. 4D representation of quinary phase diagram in 2D space[8]..... 12
Figure 2.3. Comparison of yield strength of RHEAs in the literature[6,43,45–49]. 14
Figure 2.4. Effect of the ordering on compressive behavior in Al0.5NbTa0.8Ti1.5V0.2Zr system[52]. 15
Figure 2.5. Microstructure evolution of Al10Nb15Ta5Ti30Zr40 RHEA after annealing at 1100 C (a) as-cast, and (b) annealed[55]. 16
Figure 2.6. Typical oxidation mechanisms observed in RHEA; (a) oxidation mechanism I, (b) oxidation mechanism II, (c) oxidation mechanism III, and (d) oxidation mechanism IV[65]. 19
Figure 2.7. BSE image and EDX maps of the same region in (a) as-cast, and (b) irradiated V2.5Cr1.2WMoCo0.04. 21
Figure 2.8. A schematic diagram of arc melting method[77]. 23
Figure 2.9. Interaction of powder particles and balls in high energy ball milling technique[21]. 24
Figure 2.10. Schematic drawing of SLM[89]. 26
Figure 2.11. Schematic drawing of DED system[96]. 28
Figure 2.12. (a) Low dilution or lack of fusion, (b) optimal dilution, and (c) high dilution which leads to keyholing[98]. 29
Figure 2.13. (a) Lack of fusion porosity, (b) keyhole porosity, and (c) relation between GED and porosity[98]..... 30
Figure 4.1. Property diagram of the Cr10Mo25Ta25Ti15V25 RHEA. 40
Figure 4.2. a) Optical microscopy image of the Cr10Mo25Ta25Ti15V25 showing a dendritic structure, and (b) XRD diffractogram of the alloy. 41
Figure 4.3. (a) In-situ heating XRD diffractograms up to 800 °C, and (b) XRD diffractograms of ex-situ heat treated Cr10Mo25Ta25Ti15V25 alloy up to 1200 °C. 42

Figure 4.4. First batch production of samples 1 to 8. 44
Figure 4.5. OM micrographs of (a) sample 1, (b) sample 2, (c) sample 3, (d) sample 4, (e) sample 5, (f) sample 6, (g) sample 7, and (h) sample 8. 45
Figure 4.6. XRD analysis of samples 1, 6, 7, and 8 in comparison with VAM sample. 46
Figure 4.7. SEM images of (a) sample 7, and (b) sample 8. 47
Figure 4.8. Thin wall production of samples 9, 10, and 11. 48
Figure 4.9. Thin wall production of samples 12 and 13. 49
Figure 4.10. XRD diffractogram of samples 12, 13, 14, and the upper side of sample 12. 50
Figure 4.11. Dendritic structures of (a) VAM-produced sample, and (b) DED-produced sample. 51
Figure 4.12. (a) EDX mapping showing the elemental distribution in Cr10Mo25Ta25Ti15V25 alloy, and (b) T vs. mole fraction in liquid under non-equilibrium (Scheil) condition showing segregation/depletion behavior of individual elements. 52
Figure 4.13. EDX mapping showing elemental distribution at the upper part of the RHEA. 54
Figure 4.14. (a) EBSD orientation map, (b) kernel average misorientation map, (c) grain boundary misorientation map, and (d) grain boundary misorientation map at high magnification showing submicron size grains with high angle grain boundaries. In (c) and (d), blue, green and red colors correspond to high angle grain boundaries (> 15°), low angle grain boundaries between 15°− 5° and low angle grain boundaries between 5°− 2°, respectively. 55
Figure 4.15. a) EBSD orientation map, b) pole figures, and c) inverse pole figures. 56
Figure 4.16. BFTEM images of submicron crystallite regions having (a) mostly high angle boundaries, and (b) dislocation boundaries. White arrows point the submicron crystalline regions. 57

Figure 4.17. Dislocation structures showing (a, b) dark regions of tangles and dislocation networks, and (c) linearly aligned loops. BFTEM images in (a) and (c) were taken along g < 110 > while (b) was taken along g < 002 >. 58
Figure 4.18. (a) BFTEM image showing the nano-crystalline region along the BCC zone axis of [001], and (b) HAADF image at this region showing different compositions in some of the nano-grains compared to the matrix. Inset in (a) shows the SAED pattern labeled by red (BCC-RHEA) and white (FCC-Ti) color. 59
Figure 4.19. Ti rich-FCC particles. 60
Figure 4.20. EDX maps at the heavily dislocated regions, showing a random distribution of the elements. 61
Figure 4.21. Compressive stress-strain curves of VAM and DED samples at RT. 63
Figure 4.22. Compressive stress-strain curves of VAM and DED samples at 800 °C. 64
Figure 4.23. (a) Compressive stress-strain curves of VAM and DED samples at 1000 °C, and (b) comparison of yield strength of this study with the literature [6,43,45–49]. 65
Figure 4.24. Compression test samples (a) as-prepared , (b) after RT test, (c) after 800 °C test, and (d) after 1000 °C test. 66

LIST OF ABBREVIATIONS

ABBREVIATIONS

BCC	Body Centered Cubic
DFT	Density Functional Theory
DED	Directed Energy Deposition
FCC	Face Centered Cubic
GPa	Giga Pascal
GED	Global Energy Density
HCP	Hexagonal Close Packed
HEA	High Entropy Alloy
IM	Inter Metallic Phase
P	Laser Power
MA	Mechanical Alloying
MPa	Mega Pascal
G	Powder Feed Rate
RHEA	Refractory High Entropy Alloy
Pr	Remelt Laser Power
vr	Remelt Scan Speed
v	Scan Speed
SEM	Scanning Electron Microscopy
SLM	Selective Laser Melting

TEM	Transmission Electron Microscopy
VAM	Vacuum Arc Melting
VEC	Valance Electron Concentration
XRD	X-ray Diffraction

LIST OF SYMBOLS

SYMBOLS

Å	Angstrom
ci	Atomic percentage of ith element
δ	Atomic Size Difference
$\bar{r}$	Average Atomic Radius
Sconf	Configurational Entropy
°C	Degree Celsius
ρ	Density
ΔHmix	Enthalpy of Mixing
Smix	Entropy of Mixing
K	Kelvin
Tm	Melting Point
Δx	Pauling electronegativity
ri	Radius of ith Element

CHAPTER 1

INTRODUCTION

In the pursuit of research for materials capable of withstanding the most demanding conditions, the field of refractory alloys has garnered significant attention. These alloys, characterized by their exceptional resistance to high temperatures, mechanical stress, and corrosive environments, have opened up new possibilities for applications in extreme environments. Leveraging the groundbreaking concept of high entropy alloys (HEAs), which exhibit remarkable mechanical and physical properties, this thesis delves into the development and additive manufacturing of refractory high entropy alloys, aiming to unlock their potential for extreme environment applications.

Refractory materials have long been regarded as essential components in aerospace, energy, and manufacturing industries, where operating conditions involve intense heat, aggressive chemical environments, and mechanical strain. However, traditional refractory alloys often face limitations regarding their performance and adaptability to specific requirements. The advent of high entropy alloys has provided a promising avenue for overcoming these limitations and advancing the frontiers of refractory materials.

Refractory high entropy alloys (RHEAs) offer the possibility of designing and engineering materials with enhanced thermal stability, superior mechanical strength, and excellent corrosion resistance by combining multiple refractory elements in near-equimolar proportions. This unique composition strategy and the inherent high entropy effects can yield microstructures and phase formations that exhibit extraordinary properties, surpassing those of conventional refractory alloys.

Integrating additive manufacturing techniques has revolutionized the fabrication process of refractory high entropy alloys. Additive manufacturing, also known as 3D

printing, enables the production of complex geometries and intricate structures, providing unprecedented design flexibility and efficiency. This thesis explores the desing of novel refractory high entropy alloys RHEAs and their production using both conventional techniques and additive manufacturing process to realize optimized materials for extreme environment applications.

In extreme environment applications, including high-temperature turbines, thermal barrier coatings, nuclear reactors, and aerospace propulsion systems, the demand for novel materials that can endure harsh conditions is unceasing. The development and additive manufacturing of RHEAs presents a promising avenue for meeting these challenges head-on. However, several critical aspects, such as alloy design, microstructural characterization, mechanical property evaluation, and process optimization, require comprehensive investigation to exploit the potential of RHEAs fully.

This study aims to contribute to the expanding knowledge in this burgeoning field by systematically studying the alloy composition, microstructural evolution, processing parameters, and resulting mechanical properties. Ultimately, this research endeavors to advance the understanding and utilization of RHEAs, enabling the creation of tailored materials that can thrive in the harshest of environments, leading to groundbreaking advancements in aerospace, energy, and other industries.

CHAPTER 2

LITERATURE REVIEW

The conventional strategy of alloy development consists of one main component, which has desired properties, and secondary components added either to improve those properties or to introduce new ones. This strategy allowed the discovery of many systems based on a single component. However, due to the finite number of elements on the periodic table, there are limitations in combining them to create new alloys and enhance their characteristics, along with the increase in the demand for advanced alloys started studies on multicomponent systems.

2.1 High entropy alloys

Two independent publications in 2004 by Yeh [1] and Cantor's [2] ignited researches on high entropy alloys (HEAs). These studies showed there is an unexplored domain in alloy making. Even though both studies were published in 2004, Cantor is credited as the discoverer of these alloys[3]. In his study, Cantor discovered a system with five principal elements instead of one, which resulted in an unknown alloy system. This system had an unexpected feature; it had a single-phase FCC structure[2]. Yeh et al. [4] explained this single-phase formation by stating that the high configurational entropy in the system favors the formation of single-phase structures rather than multiple intermetallic formation, thus HEAs. For the last two decades, new studies on HEAs have yielded extraordinary possibilities.

2.1.1 Definition

There are two definitions of high entropy alloys regarding their defining characteristics. These definitions are composition-based and entropy-based definition. According to composition-based definition, HEAs defined as systems composed five or more principal elements in equimolar or near-equimolar ratios [4]. While entropy-based definition considers systems magnitude of entropy. According to this definition, systems with configurational entropy higher than 1.5R are considered HEAs. HEAs are expected to obey both definitions, however there are some studies disregarding composition-based definition[5–7]. Although definitions do not consider the formation of single-phase solid solution formation is a necessity for HEAs, they are widely considered as one[8]. Therefore, there is a limited number of studies on dual phase systems[9–12].

2.1.1.1 Composition-based definition

HEAs are first defined as systems composed of at least five principal elements with equimolar ratio [4]. However, Yeh et al. extended this definition, such that HEAs are systems composed of at least five principal elements with equimolar or near-equimolar compositions, which were considered to be in the 5-35% range. In other words, 5% limit is applied to have a reasonable effect on the entropy of the system; the amounts less than, 5% considered as dopants [13].

2.1.1.2 Entropy-based definition

From the first studies, the entropy-based definition is provided based on the Boltzmann equation in Eq 2.1[4] considers the formed solutions as ideal. It is known that most of the metallic solutions are not ideal[14]; thus, the effect of temperature should be considered. However, this definition states that at high temperatures effect of temperature is minimized due to high mobility in the system[13] which results in

random distribution of the elements. Thus, this randomization allows comparison between the liquid and solid states.

$$\Delta S_{conf} = -k\, ln\, w = -R\left(\frac{1}{n}\ln\frac{1}{n} + \frac{1}{n}\ln\frac{1}{n} + \cdots\frac{1}{n}\ln\frac{1}{n}\right) = -R\ln\frac{1}{n} = R\, ln\, n \quad \text{(Eq. 2.1)}$$

Where k is Boltzmann's constant (1.380649x10^{-23} J/K), w is the number of ways of mixing or also be described as combination of components, R is the gas constant (8.314 J/K.mole), and n is the number of components[4]. According to the Boltzmann's theory, the entropy of an equiatomic alloy with five elements is 1.61R. Thus, alloys with entropies above 1.61R are considered HEAs[13]. However, some studies showed that the effect of high entropy can also be observed in quaternary alloys[6,7]. Therefore, the limit for high entropy is reduced to 1.5R[15]. The first studies show that high entropy significantly decreases Gibbs free energy of solid solutions[1,16] which leads to the formation of simple structures instead of complex intermetallic phases[4].

2.1.2 Four core effect

HEAs are generally described by these four core effects; high entropy effect, lattice distortion effect, sluggish diffusion effect, and the cocktail effect[3].

2.1.2.1 High entropy

High entropy effect, which also names these alloys, dictates solid solution formation in these systems. Since HEAs have at least five principal elements in near equiatomic compositions effect of enthalpy is reduced. Due to this reduction in enthalpy, the formation energy of intermetallic compounds also decreases. Concurrently, the system's entropy rises in line with Boltzmann's hypotheses [4]. As the number of components increases, their effect on the entropy also increases. For instance, if the number of components in different equimolar systems are 3, 5, 6, 9, then configurational entropies of these systems are 1.10R, 1.61R, 1.79R, and 2.20R, respectively. Although in real solutions, there is an effect of temperature on entropy,

solid solutions are expected to have a random distribution of elements in the structure at high temperatures[13].

2.1.2.2 Severe lattice distortion

HEAs generally form single solid solutions[17]. As a result, each atom is neighbored by different types of atoms. This variation in neighboring atoms leads to a non-symmetry brought about by differences in atomic sizes, bonding energies, and the preferred crystal structures of the constituent atoms. Hence non-symmetry causes severe shifts in atomic positions, see Figure 2.1. Thus, lattice of HEAs has a severe lattice distortion[18,19].

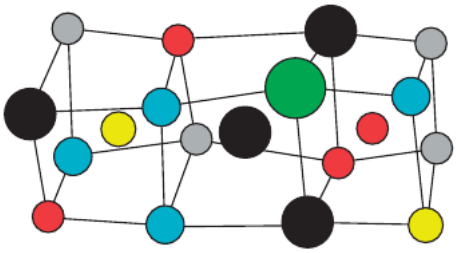

Figure 2.1. Schematic representation of severe lattice distortion in BCC alloy[20].

It is claimed that severe lattice distortion reduces the intensity of X-ray diffraction peaks, increases hardness, decreases electrical and thermal conductivity, and reduces the temperature dependence of these properties [13,17,21]. However, it should be noted that studies on the effects of other contributing factors to separate them from the influence of severe lattice distortion should be conducted to prove these claims[8].

2.1.2.3 Sluggish diffusion

Sluggish diffusion is one of the four core effects which proposes a sluggish diffusion in these systems. Although some studies show low diffusivity[22], others found no evidence of sluggish diffusion[18]. Nevertheless, diffusion in these systems is expected to be slower due to severe lattice distortion and the different elements in the system, which have different electro-negativities and bond energies. Further implication of this effect comes from the phase stability studies in these systems. Studies on phase stability of HEAs showed that even with extended heat treatments some system does not experience recrystallization or phase transformation [23–25]. Since these systems have high stored energy, they are expected to recrystallize rather quickly [3]. However, they do not have any discernable recrystallization, inferring a sluggish diffusion in the system [23–25].

2.1.2.4 Cocktail effect

Although it was first proposed by Ranganathan et al.[26] as the "Alloyed pleasures", this effect implies a synergistic mixture with an unpredictable result. This means that the proposed HEA can have either better properties than the composing elements or unexpected and undesirable outcomes. For instance, to improve the ductility of RHEAs, Nb is used[27]. However, the addition of Nb into the system can result in a decrease in oxidation resistance[28]. On the other hand, Ta can be added to the system to increase melting temperature. If this hypothetical system contains Nb together with Ta, the oxidation resistance can be improved as Ta reduces the volatility of Nb_2O_5.[29].

2.1.3 Alloy design

Alloy design is a critical part of the HEA development. Although some research is conducted on existing alloys, the main goal is to develop new grades that meet

certain requirements, such as weight reduction, high temperature strength, oxidation, etc. There are simply two different ways that can be used to design an alloy; using master alloy and computational methods.

2.1.3.1 Master alloy

This method exploits natural solid solution formation. First, possible alloying elements are selected. The number of elements can be selected down to 9 from the whole periodic table [30]. All candidate elements are added to the batch in equimolar ratios. Then production is conducted with the selected method. Later, this produced sample is analyzed to find solid solutions. Detected solid solutions are further analyzed to determine their compositions[2]. If there is any solid solution that meets the HEA criterion, that composition is re-produced to determine whether this solid solution formation is the synergetic effect of other elements in the system or it is an HEA. If the second production yields a solid solution, then the alloy design procedure is complete [30].

2.1.3.2 Computational methods

Another method used to discover new HEAs is the computational method. There are two computational steps necessary for this method. The first is empirical calculations to determine which proposed alloy systems meet the HEA criterion. If this step is successful, the second step is to do further thermodynamic calculations using calculation of phase diagrams (CALPHAD) method. This second method uses existing data of binary, ternary, and other systems to calculate properties of the proposed systems, such as phase diagrams, property diagrams, non-equilibrium cooling curves, and stoichiometry of calculated phases.

2.1.3.2.1 Empirical calculations

Initial calculations for alloy design are called empirical calculations which help to determine the ability of the constituting elements to form solid solution. Even though high entropy is required to form a solid solution, it is not the only factor governing it. For an alloy to form a solid solution, mixing enthalpy, mixing entropy, and atomic size difference should all satisfy the criteria in Table 2.1.

The equations below are used to consider whether the alloy obeys these criteria. The configurational entropy of HEAs is calculated using Boltzmann's equation. Yeh et al.[3] stated that for HEAs lower entropy limit is 1.5R. It is calculated by Eq. 2.2.

$$\Delta S_{mix} = -R \sum_{i=1}^{n} C_i \ln C_i \qquad \text{(Eq. 2.2)}$$

Where R is the gas constant, and C_i is the atomic percentage of the *i*th element [31]. Enthalpy of mixing or configurational enthalpy is determined by using Eq. 2.3.

$$\Delta H_{mix} = \sum_{1=1, j \neq i}^{n} \Omega_{ij} C_i C_j \qquad \text{(eq. 2.3)}$$

Where $\Omega_{ij} = 4\Delta H_{AB}^{mix}$ and ΔH_{AB}^{mix} is the mixing enthalpy of binary liquid AB alloy and C_j is the atomic percentage of *j*th element [31]. Zhang et al.[20] stated that configurational enthalpy should be between -15 and 5 kJ/mol.

Atomic size mismatch (δ) is defined by Eq. 2.4 as:

$$\delta = \sqrt{\sum_{i=1}^{N} C_i (1 - r_i / (\sum_{i=1}^{N} c_i r_i))^2} \qquad \text{(Eq. 2.4)}$$

Where r_i is the atomic radius of *i*th element. Zhang et al.[20] showed that δ should be smaller than 6.6%. Otherwise, the system cannot sustain a solid solution and forms intermetallic compounds.

Further studies on HEAs showed that instead of analyzing enthalpy and entropy separately, Ω which is a function of both enthalpy and entropy (Eq. 2.5) should be analyzed.

$$\Omega = T_m \Delta s_{mix} / |\Delta H_{mix}| \quad \text{(Eq. 2.5)}$$

Where T_m is the melting temperature of the alloy calculated with rule of mixture (ROM) [31]. It is shown that for a system to support a solid solution, Ω should be higher than 1.1.

Besides the criteria given in Table 2.1, other parameters such as Pauling electronegativity (Δx) and valance electron concentration (VEC) should also be considered for HEAs as shown in Eqs 2.6 and 2.7 [31].

$$\Delta x = \sqrt{\sum C_i (1 - x_i/\bar{x})^2} \quad \text{(Eq. 2.6)}$$

Where $\bar{x} = \sum_{i=1}^{n} C_i x_i$ and x_i is the Pauling electronegativity of *i*th element [31]. Although this parameter has no specified criteria, it must be low since electronegativity is an important factor for compound formation. In other words, if the system has a high electronegativity difference, it is expected to form intermetallic compounds rather than solid solutions [31].

$$VEC = \sum C_i (VEC)_i \quad \text{(Eq. 2.7)}$$

Where $(VEC)_i$ is the valance electron concentration of *i*th element [31]. This parameter is used to predict the lattice structure of the HEA. Alloys with VEC>8 form an FCC structure while the alloys with VEC<6.8 form a BCC structure[32]. However, these values are not considered to be exact. Guo et al[32]. reported that although there are some exceptions, in most cases, phase prediction with VEC is accurate.

Table 2.1 Empirical calculation criteria.

ΔS_{mix}(J/ mole. K)	ΔH_{mix} (KJ/ mole)	δ (%)	Ω
≥1.5R	-15 ≤ ΔH_{mix} ≤ 5	≤ 6.6	≥1.1

Apart from these parameters, other properties might be calculated depending on the expected properties of the designed alloy. For these calculations, the ROM is used.

Although it might deviate from actual values due to cocktail effect, ROM calculation can give an important insight during alloy design. In the context of this thesis study, density and melting temperature were also calculated using the below formula.

$$X = \sum_{i=1}^{n} C_i X_i \quad \text{(Eq. 2.8)}$$

Where X_i is the considered property of *i*th element.

2.1.3.2.2 CALPHAD method

Phase diagrams are vital tools for understanding any phase formation. Typically, phase diagrams are determined through equilibration experiments, followed by thermal analysis and characterizations. However, this technique requires a lot of experimentation and time especially for higher order systems. Therefore, computational methods are applied to determine phase diagrams.

In equilibrium conditions, phase diagrams are calculated using Gibbs free energy data. Gibbs free energy can be calculated as a function of pressure, temperature, and composition[21]. Thus, using their individual Gibbs free energies equilibrium state of the system can be calculated.

Along with existing data CALPHAD method can predict higher-order phase diagrams[3]. Figure 2.2 shows the 2D representation of the 4D quinary phase diagram. In this representation, all 5 quaternary, 10 ternary, and 10 binary diagrams are shown. Similar to the case in Figure 2.2, any higher-order system can be visualized using the lower-order systems. To be able to plot the phase diagram of a quinary system, plots of quaternary diagrams are used. If the data is incomplete, then ternary diagrams are used to plot them. If they are also incomplete, binary diagrams are used. In other words, this method calculates phase diagrams by extrapolating lower-order systems' data[33].

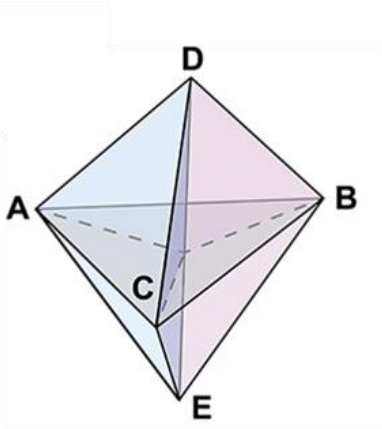

Figure 2.2. 4D representation of quinary phase diagram in 2D space[8].

On the other hand, this extrapolation can create accuracy problems for calculated phase diagrams[34]. For instance, in a hypothetical quinary system of the X alloy, accuracy diminishes when plotting three-phase diagrams using different types of data. The first diagram, relying solely on quaternary phase diagrams, demonstrates a certain level of accuracy. However, the progressive decline in accuracy will be observed when only ternary phase diagrams are used for the second diagram and exclusively binary phase diagrams for the third. Although most binary phase diagram data covering the entire spectrum of composition and temperature are complete, many ternary diagrams remain incomplete [34]. This lack of comprehensive ternary data impedes our ability to derive complete thermodynamic descriptions. So, DFT calculations are used to fill the gaps in those systems[35]. However, this can cause unreliable results, especially for low temperatures due to slow kinetics [35]. To overcome this issue, key experiments are conducted[35].

2.2 Refractory high entropy alloys

RHEAs are one of the subgroups of HEAs. These alloys are generally formed using refractory transition elements like Cr, Hf, Mo, Nb, Ta, Ti, V, W, and Zr, and non-refractory metals like Al, Co, or Ni. These alloys generally have single-phase BCC

structures. They tend to have high mechanical strength, even at elevated temperatures[36]. Due to the elements forming these RHEAs, they tend to have high melting points[7,37]. Also, some studies found that these alloys can have good oxidation [28,38] and irradiation resistance[39,40].

2.2.1 Properties

As it is explained in Part 2.1.2.4, HEAs benefit highly from the cocktail effect. Since there is an impossibly large composition range, many different effects can be observed. The properties of RHEAs will be analyzed in the scope of this thesis work.

2.2.1.1 Mechanical properties

RHEAs tend to have higher strength than conventional engineering alloys. Due to severe lattice distortion in the system and the mechanical properties of the constituting elements, yield strength is expected to be high[41]. Compressive studies on RHEAs found that the yield strength of these alloys' ranges from 900 to 2050 MPa at room temperature[42–44]. Figure 2.3 shows room temperature and high temperature compressive behavior of RHEAs in comparison with some of the other engineering alloys. It can be seen that along with high strength at room temperature, these alloys exhibit high strength at elevated temperatures. Even though all RHEAs experience a loss in yield strength, the level of reduction in yield strength changes. For instance, in AlMo0.5NbTa0.5TiZr system between 800 and 1000 °C, yield strength reduced approximately to half of the RT values[42]. On the other hand, Feng et al.[45] showed CrMoNbV system can sustain over 1100 MPa yield stress even at 1000 °C. Also, in one of the first studies on RHEAs, Senkov et al. [6] found that NbMoTaW and NbMoTaVW systems have compressive strengths above 400 MPa, even at temperatures as high as 1600 °C.

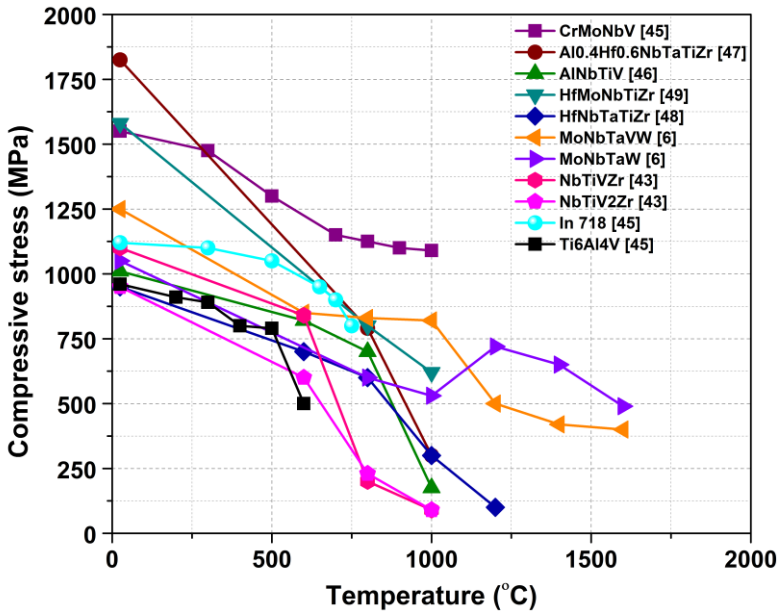

Figure 2.3. Comparison of yield strength of RHEAs in the literature[6,43,45–49].

The ductility of RHEAs is another mechanical property that should be considered. Usually, there is a compensation between ductility and strength[8] which means strength decreases with increased ductility. However, Liu et al.[50] showed that in the AlxCrFeNiTi0.25 system, ductility and strength change together in the same manner. They reported that the compressive strength and ductility are at their maximum when x=0.5, and both decrease when x increases or decreases.

Initially, the ductility of the RHEAs was thought to be guided by the VEC value. It was reported that the alloys with VEC values smaller than 4.4 are ductile while the ones with VEC values above 4.6 are brittle[51]. However, Soni et al.[52] showed that the ductility is related to the ordering in the crystal structure. In their study, Al0.5NbTa0.8Ti1.5V0.2Zr RHEA was used in three different conditions. These conditions being (1) as produced (2) one-step heat treated at 1400 °C for 20 mins, and (3) two-step heat treated at 1400 °C for 20 mins then at 600 °C for 120 hours. They have found that through heat treatment transition between ordered BCC_B2 and disordered BCC structures can be promoted. Figure 2.4 shows more disordered

sample (2) shows higher ductility while a more ordered sample (1) shows higher strength. However, in both cases, general relation between strength and ductility is observed. Sample in 3rd condition showed a better combination of ductility and strength. This combination resulted from a disordered matrix consisting of ordered particles. Even though this infers the effect of the structure ordering on the ductility instead of VEC value, there is no consensus in the community about the effect of VEC so far.

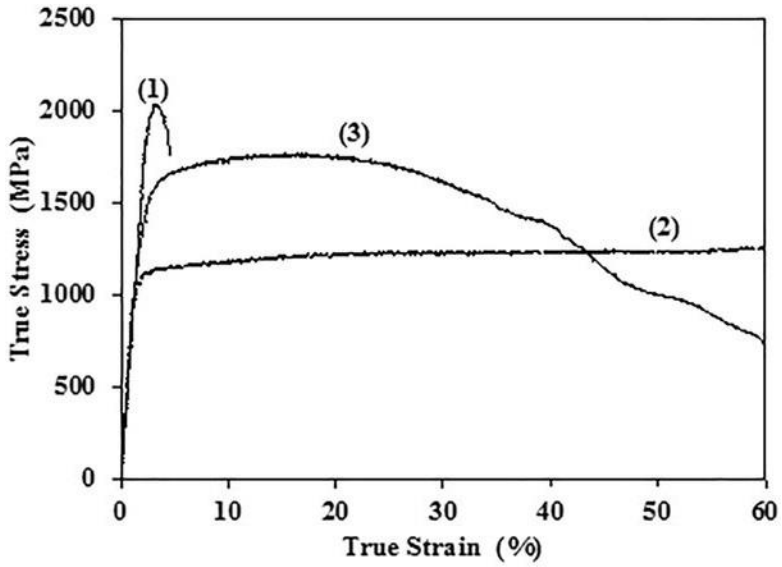

Figure 2.4. Effect of the ordering on compressive behavior in Al0.5NbTa0.8Ti1.5V0.2Zr system[52].

2.2.1.2 High temperature stability

One of the core effects of HEAs is sluggish diffusion. Secondary observations on HEAs supports this hypothesis, such as the appearance and stability of nanocrystalline structures[23,25], their inability to form low-temperature phases even at

furnace cooling conditions[24], and their ability to act as a better diffusion barrier than their conventional counterparts[22].

The resistance to diffusion plays a part in the high-temperature stability of these alloys. Due to the slow kinetics in these alloys, the recovery and recrystallization phenomena are difficult to take place. However, even though there are examples of these highly stable systems[53,54], some systems show high mobility at elevated temperatures[55]. For instance, Soni et al. studied microstructure evolution and resulting order disorder transition of crystal structure on Al10Nb15Ta5Ti30Zr40 RHEA, see Figure 2.5. Therefore, Lederer et al. [56] conducted some computational studies on RHEAs. Results show that the recrystallization temperature of RHEAs can be as high as 0.8Tm instead of 0.4Tm.

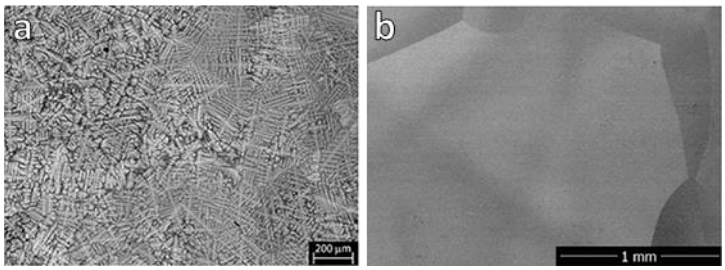

Figure 2.5. Microstructure evolution of Al10Nb15Ta5Ti30Zr40 RHEA after annealing at 1100 C (a) as-cast, and (b) annealed[55].

The high entropy effect is important for high-temperature stability. Since the theory behind HEAs is the exploitation of high entropy at elevated temperatures and immobility at low temperatures, the formed solid solution is expected to be stable[4,57]. Therefore, thermal instability of RHEAs is a concern at intermediate temperatures rather than high temperatures. Since, at these temperatures, the energy of the single atom is considerably high, their mobility can also be high. Pacheco et al. showed that HCP formation expected at 600 °C might not occur even after 1h heat treatment.

However, this transformation can occur during slow cooling from 800 and 1000°C. Also, study on oxygen-doped TiZrHfNbTa system showed that reducing the time at intermediate temperatures can prevent phase transformation[58]. Thus, for these alloys, high-temperature stability is not a concern, but medium-temperature stability is a concern.

2.2.1.3 Corrosion behavior

There is a vast knowledge of the oxidation behavior of conventional alloys. However, this knowledge barely scratches the surface of RHEAs. It is expected that due to the different components present, RHEAs can be tailored to have good corrosion resistance, in correlation with the cocktail effect, one of the core effects. However, the cocktail effect might result in something unexpected, as explained above.

In some cases, components that are added for other reasons can decrease the corrosion resistance of these systems. For instance, the formation of CrTaO4 is expected to improve oxidation resistance since it solves other oxides to form coherent oxide layers. Also, Al in the system is expected to form a protective Al2O3 oxide layer. However, Müller et al. found that in the TaMoCrAl system, existence of Mo causes complete oxidation. Thus, the synergetic effect of Mo results in the inefficiency of Al2O3 and CrTaO4 oxide layers. Therefore, together with the study of the oxidation behavior of individual elements in the system, the synergetic effects of elements in the system should be considered. Table 2.2 summarizes the oxidation behavior of the refractory elements.

Table 2.2 Oxidation behavior of refractory elements.

element	*Oxidation behavior*
Al	Protective Al2O3 former[59]
Cr	Protective Cr2O3 and CrTaO4 former[28] Neutralizes Nb2O5 by formation of NbCrO4[29]
Hf	Supports pesting by increasing oxide volumes[51]
Mo	Volatile MoO3 former[28,60]
Nb	Forms volatile polymorphic oxides[28]
Ta	Increases formation temperature of Nb2O5[29] Protective CrTaO4 former[61,62]
Ti	Supports formation of protective complex oxides[28,38]
V	Volatile V2O5 former[38,63]
W	Volatile WO3 former[64]

Gorr et al.[65] categorized the oxidation behavior of RHEAs into four mechanisms, as shown in Figure 2.6. The first two mechanisms are severe oxidation mechanisms. In mechanism I, see Figure 2.6.a, excess rapid oxide formation and growth occurs due to high oxygen solubility or internal cracking of the oxide layer. This results in the exfoliation of outer layer oxide. A study by Chang et al.[66] shows this mechanism in TiZrNbHfTa alloy.

In mechanism II, see Figure 2.6.b, the fast growth of oxide scales occurs. These scales are usually porous and allow inward oxygen diffusion at high rates. Exfoliation of these oxide scales often occurs. A study by Müller et al.[28] shows this mechanism in NbMoCrTiAl alloy.

In mechanism III, see Figure 2.6.c, relatively protective oxide layers are formed. Unlike previous mechanisms formed oxide layer grows slowly. For instance, the CrTaO4 oxide layer shows this behavior. The key feature of this oxide is to prevent

oxygen and metal diffusion and solve any oxides formed at the surface. Several studies showed the protective capabilities of this mechanism[61,62].

In mechanism IV, see Figure 2.6.d, the highest oxidation resistance is achieved. The most notable example of oxide obeying this mechanism is Al2O3. However, achieving this high level of protection is rather rare. This mechanism was only observed in the study of Ghadyani et al.[59]

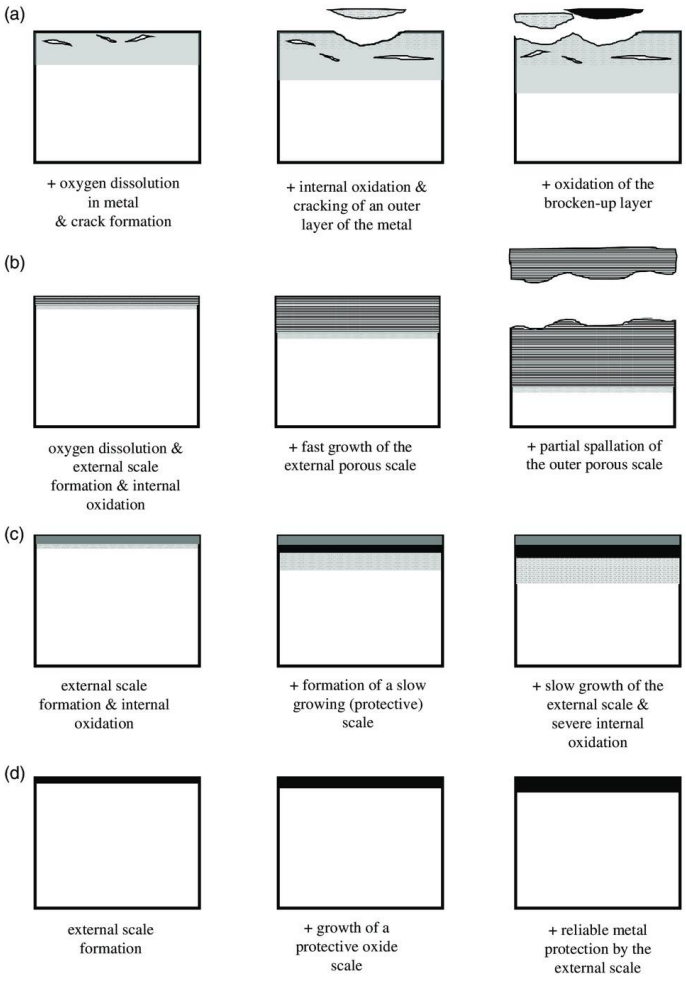

Figure 2.6. Typical oxidation mechanisms observed in RHEA; (a) oxidation mechanism I, (b) oxidation mechanism II, (c) oxidation mechanism III, and (d) oxidation mechanism IV[65].

2.2.1.4 Irradiation resistance

RHEAs are notable for their potential resistance to radiation damage, an essential characteristic when materials are subjected to intense radiation[67]. In environments like nuclear reactors, materials encounter consistent neutron bombardment, resulting in atomic displacements and the formation of point defects and defect clusters[67,68]. Such defects, over time, can cause materials to become brittle, swell, and have reduced thermal conductivity[68].

The inherent high entropy and distinct microstructure of RHEAs make them particularly resistant to radiation-induced degradation[69]. Some studies even suggest that certain RHEAs could serve as future structural materials in nuclear systems due to this resistance[70–73]. For example, research by Waseem et al.[74] showed that the irradiation hardening for a pure W was 28.79% at 5.5 dpa, whereas that for the W0.5(TaTiVCr)0.5 RHEA was 17.27% at 6.5 dpa, both irradiated with Fe ions at room temperature. Another study by Sadeghilaridjani et al.[75] compared the mechanical properties of the HfTaTiVZr RHEA with the SS304 conventional alloy. Both were irradiated with Ni ions at room temperature up to 40 dpa. The results showed that irradiation hardening in the HfTaTiVZr alloy was 13%, while it was 50% in SS304.

In another study, Patel et al.[76] used Au ions to irradiate a V2.5Cr1.2WMoCo0.04 RHEA at room temperature up to 40 dpa. Analysis using an energy dispersive X-ray (EDX) spectrometer in SEM, shown in Figure 2.7, revealed that irradiation did not lead to elemental segregation in the alloy, indicating good phase stability even at an irradiation damage level of 40 dpa. These findings underscore the promise of RHEAs as resistant materials in high-radiation environments.

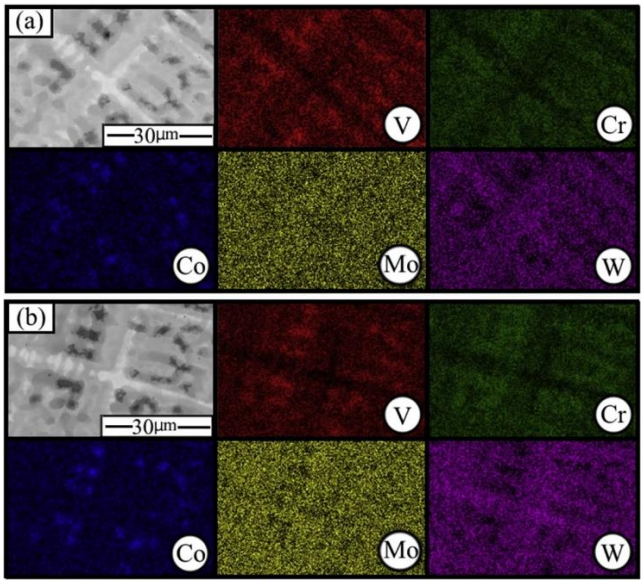

Figure 2.7. BSE image and EDX maps of the same region in (a) as-cast, and (b) irradiated V2.5Cr1.2WMoCo0.04.

2.3 Production methods of RHEAs

Even the slightest impurity can have a synergistic effect, potentially leading to undesirable outcomes. As a result, the production of RHEAs necessitates the use of high-purity raw materials. Given this requirement, all production methods typically employ either a controlled atmosphere or a shielding gas. Commonly used methods for RHEA production include vacuum arc melting (VAM), mechanical alloying followed by material consolidation, and additive manufacturing. Among these production methods, fusion-based additive manufacturing techniques, such as SLM (Selective Laser Melting) and DED (Directed Energy Deposition), stand out for their ability to produce large-scale and intricately shaped components. In contrast, VAM is typically limited to producing smaller billets of the alloy. If solid state production is taken into consideration, mechanical alloying is applied. Although VAM method allows the small sized components, it is the dominant method of production used in research on RHEAs.

2.3.1 Vacuum Arc Melting

Vacuum arc melting is the most popular method for RHEA production. In this technique, all constituting elements are placed in a copper crucible and melted down with a torch reaching up the temperatures above 3000 °C. The torch temperature can be adjusted depending on the constituting elements. For instance, using high temperatures above 3000 °C can cause evaporation of pure Cr. Although torch temperature is adjustable, it is not suggested to use the VAM method for elements like Zn and Mg. Since their boiling point is too low, controlling the concentration is challenging. However, for refractory metal production, this method is a practical choice. Therefore, VAM has been the most popular method since their discovery by Senkov et al.[7].

Figure 2.8 shows schematic of a VAM system. The raw materials are placed into the copper crucible. Then chamber preparation is done by vacuuming and flushing with argon gas three times to reduce oxygen concentration to negligible levels. After that chamber is filled with Ar gas to positive pressure which ensures to keep the atmosphere concentration constant. Melting of the constituents are done by creating a high-temperature torch using an electric current. To ensure the complete melting of the refractory elements, the batch is turned upside down a few times and remelting is applied. Furthermore, mold can be used with a suction attachment instead of a crucible. This way, produced samples can be molded into simple shapes like rods, sheets, or cones.

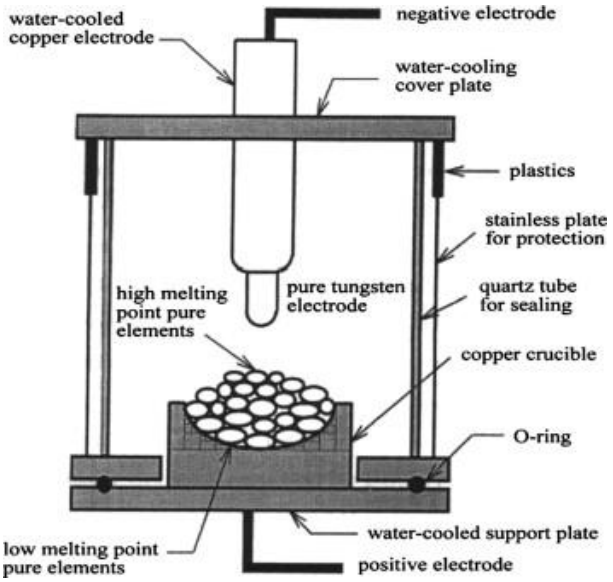

Figure 2.8. A schematic diagram of arc melting method[77].

VAM production results in a typical dendritic microstructure with interdendritic segregations[3,78]. Depending on the cooling rate, dendrite size changes. High cooling rates result in fine dendrites, while slow cooling rates result in course dendrite formation. Bashev et al. [79] showed that ultra-fine disordered structures can be formed due to ultra-rapid solidification.

2.3.2 Mechanical alloying and material consolidation

2.3.2.1 Mechanical Alloying (MA):

Mechanical alloying is a technique for preparing metal powders, utilizing high-energy ball mills to induce cold welding, fracturing, and rewelding of the powders through interaction of powder particles and balls[21], see Figure 2.9. The high energy applied during the process enhances the solid solubility driving force of HEAs, resulting in homogeneously alloyed powders. Key parameters in this process include milling time, ball-to-powder ratio, and mixing speed[78]. Low mixing speed is

insufficient to achieve the requisite high energy, preventing mechanical alloying from occurring. Considering ball-to-powder ratio, even though increasing the number of balls in the system amplifies the applied energy, an overly high ball to powder ratio inhibits the powders from welding together to create solid solutions[80]. Moreover, insufficient milling time can lead to uneven solid solution formations, causing the resultant milled powders to deviate from those prepared through alternative methods. The research by Zhang et al. [81] reported that chemically homogeneous powders with refined morphologies can be produced with adequate milling time.

Studies have demonstrated the viability of RHEA production via this approach [80,82–84]. Given that mechanical alloying avoids ultra-high temperatures and yields chemically consistent powders, it stands as a viable alternative to traditional methods.

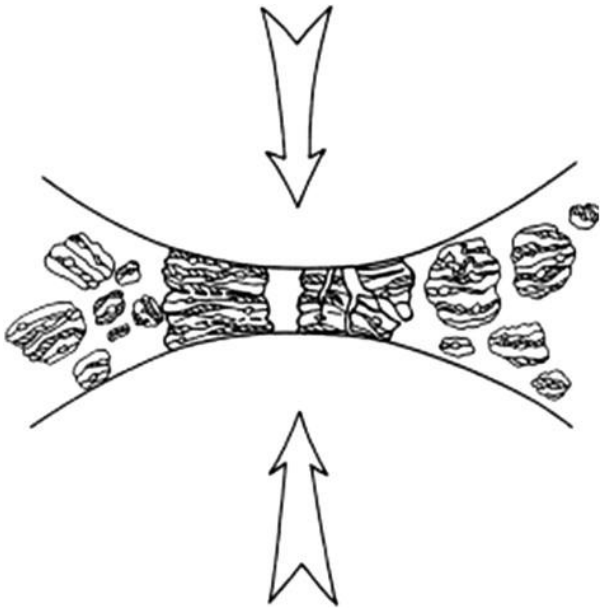

Figure 2.9. Interaction of powder particles and balls in high energy ball milling technique[21].

2.3.2.2 Consolidation

After the mechanical alloying process, a consolidation method is essential to achieve bulk material. There are two methods generally used for consolidation which are hot isostatic pressing (HIP) and cold pressing and sintering. HIP melds powders into the desired form by applying both heat and pressure. The pressure helps compact the powders and eradicate any structural porosities, while the heat enables sintering. Given the concurrent application of heat and pressure, the powders soften, and less force is necessary for optimal consolidation. Additionally, the applied pressure bolsters the powders' sintering rate, with both heat and pressure working synergistically for maximum consolidation. Alternatively cold pressing and sintering can be used as a consolidation method. in which heat and pressure are applied sequentially. Consequently, the pressures and sintering durations needed are higher compared to HIP.

2.3.3 Additive Manufacturing

2.3.3.1 Selective Laser Melting

Selective Laser Melting (SLM) is an additive manufacturing technique based on powder bed fusion. In this process, a uniform layer of powder is laid either on a base substrate or atop a prior layer. A laser beam then targets and melts the powder in a CAD model-defined pattern. As the laser traces the designated geometry, the powder is fused or welded to create a solid structure. Once a layer is complete, the build platform lowers, and a fresh layer of powder is spread across the surface with recoater, and the process repeats, see Figure 2.10. Precision in SLM relies heavily on adjusting several parameters, including laser power, scan speed, layer depth, hatch spacing, and the scan rate[85–87]. Given the reactive nature of powders used in RHEA production, SLM is conducted inside a sealed chamber filled with a non-reactive gas, like argon or nitrogen.

The optimized parameters, coupled with high-quality powders, ensure dimensionally accurate components with a consistent microstructure. However, as a characteristic of powder bed techniques, SLM uses more powder than the size of the final product. The entire bed needs to be filled, irrespective of the deposition area, to maintain the product quality, see Figure 2.10. This requires not only more powder than the end product but also pre-alloying[88]. Considering the high costs of the refractory raw materials, SLM production of the RHEAs require large initial investment compared to the DED technique.

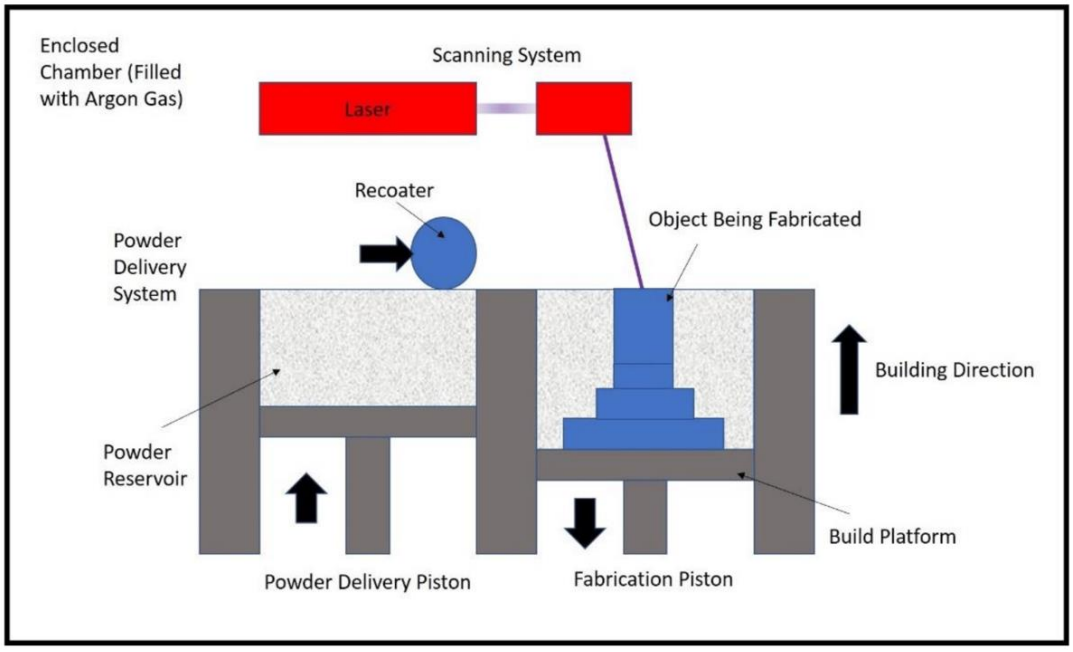

Figure 2.10. Schematic drawing of SLM[89].

2.3.3.2 Directed Energy Deposition

Directed Energy Deposition (DED) operates based on the principle of concentrating energy, often from a laser beam, onto a specific point where metal particles are melted and then solidified. The intensity of laser significantly influences resolution

of the prints, whereas the fabrication speed of DED determines the deposition rate[85,90].

Unlike the SLM method, where powder is spread out in a bed before melting, DED continually feeds metal powder to the area targeted for deposition[91]. As it can be observed from Figure 2.11 during DED procedure powder is fed through coaxial nozzle along with laser. This powder feed melted after blown through nozzle and deposited on the substrate.

While DED can utilize pre-alloyed powders, they are not mandatory. The direct spray of the powder alongside the laser onto the target allows for on-the-spot alloying. This method allows the use of multiple hoppers with distinct feeders, which is especially advantageous for fabricating RHEAs. By utilizing elemental powders as feedstock, there's no need for pre-alloyed powders[88]. Moreover, by precisely controlling the powder supply from various hoppers and optimizing processing conditions, it's possible to create materials that are either chemically homogeneous or have a compositional gradient through in-situ alloying[92,93]. Given the substantial material costs of refractory metals, choosing a mixed powder over a pre-alloyed one can be more cost-effective. Yet, due to the varying melting points of RHEAs' constituent elements, a subsequent remelting process is crucial[92,94,95]. This step ensures the melting of the powder fully, leading to the intended RHEA formation. DED is especially notable for its low energy consumption and ability to produce large samples, an advantage for both research and industrial purposes.

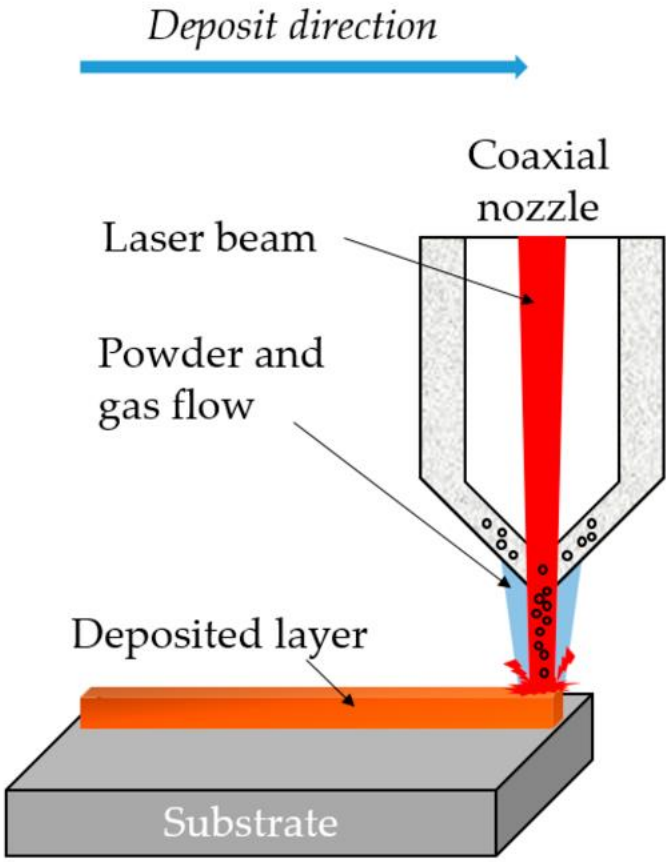

Figure 2.11. Schematic drawing of DED system[96].

DED harnesses the ability of materials to establish metallurgical bonds by creating melt pools during deposition. This ensures the interconnection of each layer with the one previously deposited [97]. To ensure optimal bonding between consecutive layers, a specific threshold of metallurgical bonding is essential. This can be quantified through a dimensionless parameter known as dilution [98]. Dilution is determined using Eq. 2.9.

$$D = \frac{d}{h+d} \qquad \text{(Eq. 2.9)}$$

Where *h* is the deposition height, and *d* is the depth of the melt pool created below deposition surface[98]. A high *h* value leads to low dilution and a subsequent lack of fusion between layers. Conversely, a high *d* value results in elevated dilution and the occurrence of the keyholing phenomenon. Figures 2.12a and c depict low and high dilution levels, respectively while Figure 2.12b illustrates an optimal dilution range of 10% to 30%[98], which fosters excellent metallurgical bonding.

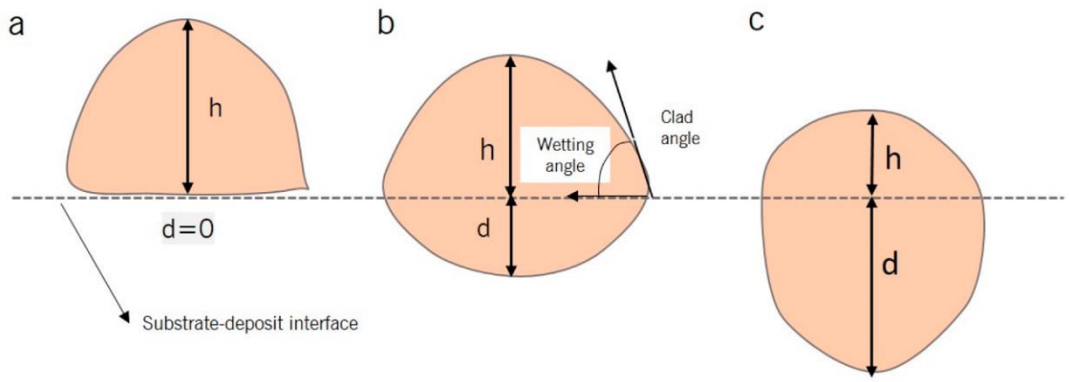

Figure 2.12. (a) Low dilution or lack of fusion, (b) optimal dilution, and (c) high dilution which leads to keyholing[98].

The Global Energy Density (GED) is pivotal in DED, playing a central role in ensuring the high-quality production of materials. There is a direct correlation between GED and dilution. Factors that impact GED include laser power, scanning speed, spot size, and the rate of powder deposition, as shown in Eq. 2.10.

$$GED = \frac{P}{G \times v \times d_{beam}^2} \qquad \text{(Eq. 2.10)}$$

Where P is laser power, G is powder flow rate, v is scanning speed and d_{beam} is laser spot diameter[98]. As presented in Figure xc, lower GED values correspond to reduced dilution, increasing the risk of lack of fusion porosity[99],see Figure 2.13a. On the other hand, elevated GED values result in significant dilution, heightening the propensity for keyhole porosity[100],see Figure 2.13b. Thus, carefully controlling GED is imperative to achieve optimal building height and minimize porosity. Figure 2.13c shows relation between GED and porosity. This figure shows overall porosity level can be optimized changing GED according to the observed porosity type. However, it should be noted that production parameters are material dependent.

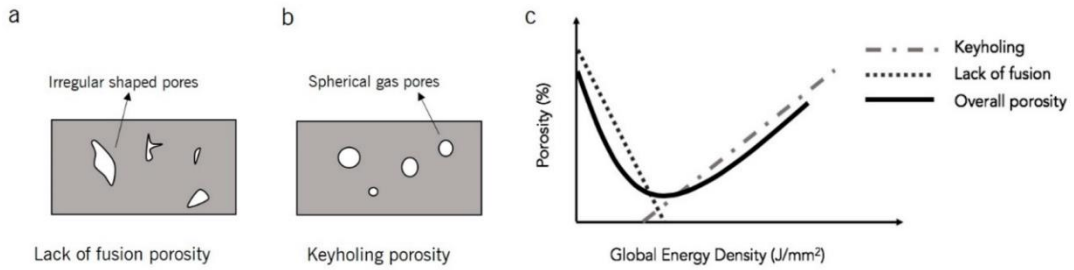

Figure 2.13. (a) Lack of fusion porosity, (b) keyhole porosity, and (c) relation between GED and porosity[98].

CHAPTER 3

METHODS AND EXPERIMENTAL PROCEDURE

3.1 Alloy design

The first step in the alloy design was determining its composition. The study's objective was to develop a novel RHEA characterized by high-temperature stability and robust compressive strength. Therefore, element selection was based on refractory metals, considering factors like their densities, melting temperatures, thermal conductivities, valence electron concentrations (VEC), and the synergetic effects observed in previous studies.

3.1.1 Empirical calculations

Empirical rules for solid solution formation were used to assess solid-solution formation probability of designed alloys. For this purpose, atomic size difference (Eq.1), mixing enthalpy (Eq. 2), mixing entropy (Eq.3), electronegativity difference (Eq.4) and VEC (Eq.5) are the important parameters to consider for solid solution formation [31]. Elemental parameters were obtained from Entall data base[101].

$$\delta = \sqrt{\sum_{i=1}^{n} c_i \left(1 - {r_i}/{\bar{r}}\right)^2} \qquad \text{(Eq. 3.1)}$$

Where $\bar{r} = \sum_{i=1}^{n} c_i r_i$, c_i and r_i are the atomic percentage and atomic radius of the ith element, respectively [31].

$$\Delta H_{mix} = \sum_{i=1, i\neq j}^{n} \Omega_{ij} c_i c_j \qquad \text{(Eq. 3.2)}$$

Where $\Omega_{ij} = 4\Delta H_{AB}^{mix}$ and ΔH_{AB}^{mix} is the mixing enthalpy of binary liquid AB alloy [31].

$$\Delta S_{mix} = -R \sum_{i=1}^{n} c_i ln c_i \quad \text{(Eq. 3.3)}$$

Where R is the gas constant [31].

$$\Delta x = \sqrt{\sum_{i=1}^{n} c_i (x_i - \bar{x})^2} \quad \text{(Eq. 3.4)}$$

$\bar{x} = \sum_{i=1}^{n} c_i x_i$ and $x_i$is the Pauling electronegativity of *i*th element [31].

$$VEC = \sum_{i=1}^{n} c_i (VEC)_i \quad \text{(Eq. 3.5)}$$

Where $(VEC)_i$ is the VEC for the *i*th element [31].

3.1.2 CALPHAD

To ascertain the phases and their fractions under both equilibrium and non-equilibrium conditions, the CALculation of PHAse Diagram (CALPHAD) method was utilized via the ThermoCalc software. The CALPHAD approach computes Gibbs Free energy versus composition plots for all conceivable phases across elemental, binary, ternary, quaternary, and quinary systems. Using this data, phase diagrams can be generated, enabling the determination of critical temperatures for phase transformations in any HEA system[102,103]. The study employed the ThermoCalc database of TCHEA6 v2022a, which encompasses 20 elements with information on over 400 possible phases[104]. Additionally, Scheil calculations were executed to project the non-equilibrium phase diagram and potential structural alterations, such as partitioning during solidification.

3.2 Production methods

The Cr10Mo25Ta25Ti15V25 RHEA was Produced using both vacuum arc melting (VAM) and directed energy deposition (DED) techniques. VAM served as a means for initial characterization, providing insights into the alloy's behavior following a conventional production method. On the other hand, DED was employed to assess the alloy's suitability for additive manufacturing, especially in the context of using a single hopper for mixed powder production.

3.2.1 Vacuum Arc Melter

The Compact Arc Melter MAM-1 was used to produce the alloy. Granules of Cr (99.9 wt.%), Mo (99.95 wt.%), Ta (99.9 wt.%), Ti (99.99 wt.%) and V (99.7 wt.%) were combined and placed into the arc melter. Prior to each melting phase, the chamber underwent a vacuum process and was subsequently flushed with Ar gas a minimum of three times. To achieve complete mixing and melting of the elements, the produced beads were flipped and subjected to remelting multiple times, specifically at least seven times. For the purpose of compression tests, these beads were cast into a Cu mold measuring 5 mm in diameter and 30 mm in length. This was done using a suctioning aperture attached to the mold. Given the high melting temperature of the RHEA and the rapid cooling rate due to cooling water, the samples were not intended to occupy the entire mold. Instead, they filled only two-fifths of it to ensure optimal casting. To eliminate the possibility of slag inclusion, the ends of the cast samples were removed.

3.2.2 Directed Energy Deposition

DED was performed using a DMG-Mori Hybrid system with an Nd:YAG laser having a maximum power of 2500 W and a spot diameter of 3 mm. Cr (99.9 wt.%), Mo (99.95 wt.%), Ta (99.9 wt.%), Ti (99.99 wt.%), and V (99.7 wt.%) powders with

a particle size of 50–110 μm of were mixed under an Ar atmosphere and placed in the feeding hopper. An isolation chamber was built to control process atmosphere. The chamber had an outlet to compensate for incoming carrier gas and protection gas. Protection gas was blown into the chamber through an inlet at the bottom of the isolation chamber. The chamber was equipped with an Apogee SO-421 SDI-12 oxygen sensor with a sensitivity of 10 ppm to measure the oxygen level in the isolation chamber. Before every production chamber was purged with Ar until the oxygen level dropped below 10 ppm.

In the first batch, for parameter optimization, 8 different parameters were used; see Table 4.1. The first set of parameters was used to determine the capacity of powder deposition. For this purpose, 3 layers of 5-cm-long single-track depositions with deposition height of 1.12 mm were conducted on a steel substrate at room temperature under Ar atmosphere.

Table 3.1 Production parameters used for first batch.

Sample #	*1*	*2*	*3*	*4*	*5*	*6*	*7*	*8*
P (W)	2000	2500	500	800	500	500	800	800
Pr (W)	-	-	-	-	2000	2500	2000	2500
v (mm/min)	750	750	400	400	400	400	400	400
vr (mm/min)	-	-	-	-	750	750	750	750
G (g/min)	15	15	10	10	10	10	10	10
# of remelt					1	1	1	1

The second set was to determine whether it is possible to fuse all unmolten powders with the deposition to form homogeneous samples. For the second batch, sample parameters 9 to 14 were used to determine production parameters, see Table 4.2. For this purpose, 3 cm-long thin walls were produced on a steel substrate at room

temperature under Ar atmosphere. Further productions of thin walls were conducted using the determined parameters.

Table 3.2 Production parameters used for second batch.

Sample #	*9*	*10*	*11*	*12*	*13*	*14*
P (W)	800	800	800	2000	2000	2000
Pr (W)	2500	2500	2500	2000	2000	2000
v	400	400	400	400	400	500
Vr	750	750	750	750	750	1000
G (g/min)	10	10	10	10	10	10
# of remelt	1	2	3	2	1	1

3.3 Characterization methods

3.3.1 X-Ray Diffraction

After production, the samples underwent phase analysis using X-ray diffraction (XRD) at a scan rate of 1°/min on a Bruker D8 X-ray Diffractometer. Phase stability was assessed both in-situ and ex-situ. For the in-situ XRD analysis, a sample measuring 1 cm × 1 cm x 0.7 mm was tested at room temperature, and then at 400°C, 600°C, and 800°C. Each temperature test was conducted with a heating rate of 10°C/min, and the sample was maintained at the specified temperature for 2 hours under nitrogen atmosphere to achieve homogenization. Ex-situ XRD evaluations were performed on samples that had been annealed at 800°C, 900°C, 1000°C, 1100°C, and 1200°C for 2 hours in an Ar atmosphere. These samples were then air quenched to room temperature to retain any potential high-temperature phases within their microstructure. All XRD measurements proceeded at a 1°/min scan rate on a Bruker D8 X-ray Diffractometer.

3.3.2 Microstructure Analysis with Optical Microscopy

VAM and DED samples underwent a grinding and polishing process down to 0.04 μm colloidal silica, and were then etched using a solution mix of 2 HF: 2 HCl: 1 HNO3. The microstructure was analyzed employing optical microscopy technique. For pore analysis images from polished surfaces were used. For optical microscopy, both the Huvitz HDS 5800 digital microscope and the Nikon ECLIPSE E200 were employed.

3.3.3 Microstructure Analysis with Scanning Electron Microscopy

The microstructure of the beads was extensively analyzed using optical microscopy and scanning electron microscopy (SEM) techniques. After being ground and polished to a finish of 0.05 μm colloidal silica, the beads were etched with a solution mix of 2 HF: 2 HCl: 1 HNO3. For the SEM analyses, a FEI Nova Nano SEM 430, fitted with an EDAX SSDD Apollo10 EDX camera, was employed.

3.3.4 EBSD Analysis

Electron backscatter diffraction (EBSD) analyses were conducted using the FEI Nova Nano SEM 430 equipped with a Hikari EBSD detector. These analyses were performed at 20 kV. For broader areas measuring either 500 μm x 500 μm or 750 μm x 1000 μm, a 1–2 μm step size was adopted, whereas for the more detailed scans on 50 μm x 50 μm areas, a finer 200 nm step size was employed for VAM samples. In addition, 3-mm TEM disks of VAM samples underwent preparation through jet electropolishing using a 5 vol% perchloric acid and 95 vol% methanol solution at a temperature of −40 °C and an applied voltage of 18.5 V. EBSD scans were subsequently carried out on these disks. Furthermore, EBSD samples of DED were prepared by mechanical polishing down to a 0.04 μm colloidal silica. EBSD analysis was conducted on the 1700 μm x 1700 μm area with 1 μm step size.

3.3.5 TEM Analysis

Transmission electron microscopy (TEM) analyses were conducted using both the JEOL JEM-ARM200CFEG UHR-TEM and the JEOL JEM-2100 F TEM. For one set of VAM samples, the JEOL JIB-4601 F MultiBeam Focused ion beam (FIB)/SEM system was employed in their preparation. Additionally, 3-mm TEM disks of VAM samples were crafted by jet electropolishing, utilizing a solution composed of 5% perchloric acid and methanol. This process was conducted at a temperature of −40 °C, with an applied voltage of 18.5 V. In another approach, 3-mm TEM disks of DED samples were initially shaped with the Fischione Model 200 dimple grinder and subsequently refined through ion milling using the Gatan 691 PIPS.

3.4 Compression tests

3.4.1 Sample preparation

The mechanical properties of the developed alloy were assessed through compression tests. Molded rods of VAM samples were prepared with a height-to-diameter ratio of 1–1.5, adhering to standard compression testing protocols. Additionally, cylindrical DED samples with dimensions of 1.5 mm radius and 1.5 mm height were precisely cut from upper parts of thin walls using electro discharge machining (EDM). Sample dimensions are given in Table 3.3.

Table 3.3 Compression test sample dimensions.

Production method	*Test temperature (°C)*	*Height (mm)*	*Diameter (mm)*
VAM	RT	8 ± 0.2	5 ± 0.1
VAM	800	2.2 ± 0.05	1.5 ± 0.01
VAM	1000	2.2 ± 0.05	1.5 ± 0.01
DED	RT	1.5 ± 0.02	1.5 ± 0.01
DED	800	1.5 ± 0.02	1.5 ± 0.01
DED	1000	1.5 ± 0.02	1.5 ± 0.01

3.4.2 Test setup

Tests were conducted using an Instron uniaxial tension/compression system equipped with a furnace. For room temperature tests steel compression apertures were used and to avoid friction machine oil was used. For high temperature tests In913 rods were used as apertures. To avoid embedding of samples to Inconel rods WC pieces were attached to the rods. Moreover, to avoid friction BN powder with 100 μm size were used.

3.4.3 Test parameters

Compression tests on the alloy were performed both at room temperature (RT) and at elevated temperatures of 800°C and 1000°C. The strain rate of 10^{-4} s^{-1} was used to achieve results that are comparable with those found in the literature[8,105,106]. For the high-temperature tests, samples were positioned in a preheated furnace for around 20 minutes to achieve a stable thermal state. It should be noted that three samples were tested for each specified condition.

CHAPTER 4

RESULTS AND DISCUSSION

4.1 Alloy Design

Refractory metals like W, Ta, and Mo are known for their high melting temperatures, while V, Zr, and Ti are favored for their reduced density. Empirical calculations have determined that CrMoTaTiV system is the optimal choice, meeting criteria for high melting temperature, low density, and an ideal VEC value that ensures satisfactory ductility. However, CALPHAD calculations on the quinary CrMoTaTiV alloy indicated that excessive Cr can lead to the formation of the Laves phase, which can cause embrittlement[43]. To circumvent this, the Cr content is limited to 10%. The final stoichiometry of the alloy is adjusted to Cr10Mo25Ta25Ti15V25, ensuring the highest melting temperature and lowest density. The thermophysical properties of this alloy, derived from empirical calculations, can be found in Table 4.1.

Table 4.1 The calculated thermophysical properties of Cr10Mo25Ta25Ti15V25 alloy.

Alloy	ρ (g/cm^3)	δ	ΔH_{mix} (kJ/mol)	VEC	ΔS_{mix} (J/K•mol)	T_m (K)	Ω	Structure
Cr10Mo25Ta25Ti15V25	9.96	2.94	-3.42	5.2	12.93	2583	9.76	BCC

Figure 4.1 shows the phase diagram in equilibrium conditions. CALPHAD analysis suggests that a single-phase BCC#2 structure is stable above ~1200 °C. However, below 1200 °C, a secondary BCC structure (BCC#1) co-exists with BCC#2. Besides, a small amount of HCP phase is predicted to form below ~200 °C.

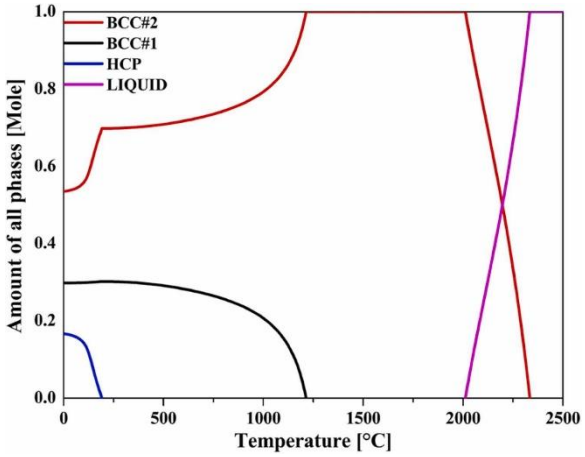

Figure 4.1. Property diagram of the Cr10Mo25Ta25Ti15V25 RHEA.

4.2 Characterization of VAM samples

4.2.1 Microstructure

Following the VAM production, a dendritic microstructure was observed due to rapid cooling. As illustrated in Figure 4.2a, there's a noticeable refinement in dendrite size towards the bottom of the sample, as highlighted by an arrow. Since samples were cooled from bottom cooling rate was higher at the bottom of the sample. Further SEM analysis did not reveal any other change in the microstructure

4.2.2 Phase analysis

XRD analysis revealed that the Cr10Mo25Ta25Ti15V25 alloy exhibits a single-phase BCC phase, deviating from the equilibrium CALPHAD calculations, see Figure 4.2b. This anomaly can be attributed to the rapid cooling experienced by VAM samples. Such a cooling rate means that the sluggish diffusion mechanism prevents any solid-state phase transformations. Consequently, instead of observing the emergence of other BCC and HCP phases, the high-temperature phase becomes

supersaturated, resulting in a single-phase at room temperature. This phase's lattice parameter is measured to be 3.18 Å.

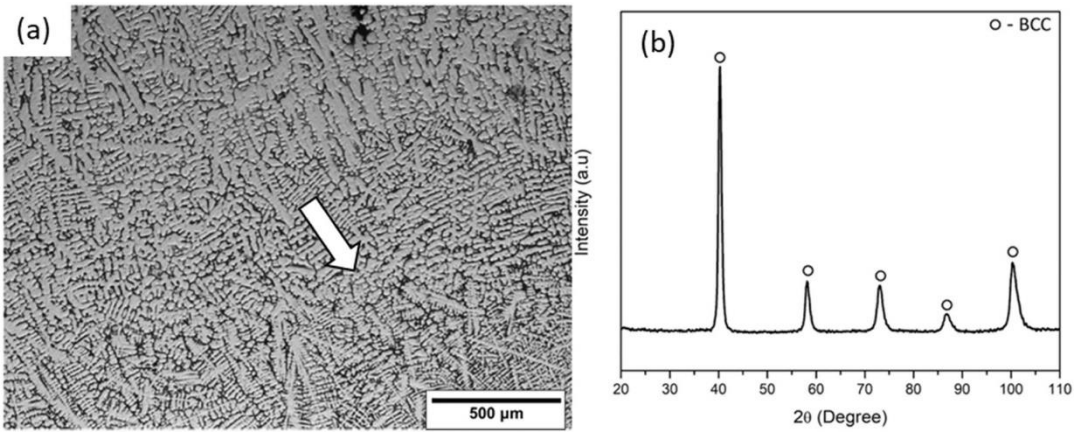

Figure 4.2. a) Optical microscopy image of the Cr10Mo25Ta25Ti15V25 showing a dendritic structure, and (b) XRD diffractogram of the alloy.

The microstructural stability of the Cr10Mo25Ta25Ti15V25 alloy at high temperatures is crucial, given its design to operate under such conditions. Consequently, in-situ and ex-situ XRD tests at high temperatures were undertaken. Figure 4.3a presents in-situ XRD diffractograms at diverse temperatures: room temperature, 400°C, 600°C, and 800°C. Notably, a phase transformation becomes apparent around 600°C, which is identified as the emergence of a secondary BCC (BCC#1) phase with a slightly enlarged lattice parameter of 3.23 Å. There's also a noticeable decline in intensity at elevated temperatures, attributable to atomic vibrations diminishing the signal-to-noise ratio[107]. The ex-situ XRD analyses, extending up to 1200°C, are depicted in Figure 4.3b. In contrast to the in-situ observations, the phase transformation discerned at 600°C occurs approximately at 1000°C, marked by minor peak shifts to smaller diffraction angles. Such variations in phase transformation temperatures in HEAs can be ascribed to their distinct diffusion mechanisms [107]. Given that the kinetics in these alloys hamper fast

diffusion, the method of heat treatment considerably impacts the transformation temperature. For instance, during the in-situ study, samples were initially heated to 400°C at a rate of 10°C/min, maintained at this temperature for 3.5 hours (inclusive of 1.5 hours of diffraction), and subsequently heated to 600°C for another 3.5 hours. Evidently, prolonged durations at lower temperatures facilitate the transformation to low-temperature phases. On the other hand, in the ex-situ tests, samples were directly heated to their respective heat treatment temperatures, sustained for 2 hours, and then quenched. This methodology delays the phase transformation to higher temperatures.

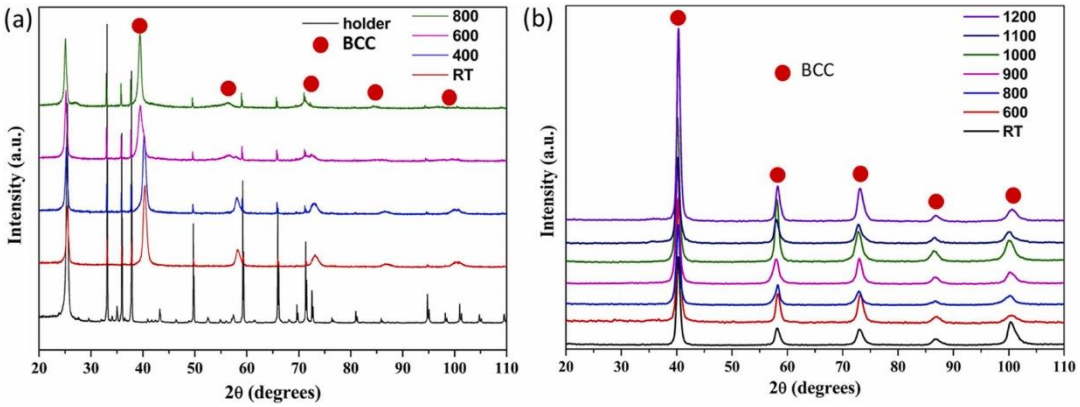

Figure 4.3. (a) In-situ heating XRD diffractograms up to 800 °C, and (b) XRD diffractograms of ex-situ heat treated Cr10Mo25Ta25Ti15V25 alloy up to 1200 °C.

4.3 Characterization of DED samples

4.3.1 Parameter optimization

4.3.1.1 First batch production

Parameters in additive manufacturing play a critical role. This study sought to optimize these parameters to produce Cr10Mo25Ta25Ti15V25 RHEAs using the

DED additive manufacturing technique. The initial production was carried out based on the parameters listed in Table 3.1. The first four parameters were evaluated for their influence on powder deposition capability. Parameters 1 and 2 were selected to analyze whether it is possible to produce this alloy only through deposition. If these parameters were sufficient for production this would allow continuous production of any shape desired to produce within the physical limitations of DED system. Parameters 3 and 4 are selected to determine deposition capability of alloying elements in this system. It should be noted that it was not expected to obtain fully homogeneous single phase alloys production with no unmolten powders, due to low energy density applied. However, these two parameters are selected to observe whether it is possible to deposit this powder mixture to further remelting steps. To analyze effect of remelting parameters 5 to 8 were selected. There were two different deposition laser power and two different remelting laser power used. Two selected deposition laser powers were the 500 W and 800 W which are also used in samples 3 and 4 respectively without remelting step. This allowed to investigate effect of deposition laser power on remelting step. Two selected remelting laser powers were 2000 W and 2500 W which were also used in samples 1 and 2 respectively as a deposition parameter. Each different remelting power were applied to 500 W and 800 W deposits to analyze better combination of these parameters.

Initial production trials revealed challenges in producing this alloy solely through the deposition step, given the differing melting temperatures and laser absorption rates. An initial examination of powder deposition using the parameters 1 to 4 in Table 3.1 without any remelting step revealed that samples 1 and 4 achieved adequate deposition. In contrast, sample 3 suffered from lack of fusion, while sample 2 became embedded into the substrate, resulting in no discernible deposition height. Further analysis on sample 1 indicated a significant crack formation at the interface between the deposit and substrate. On the other hand, sample 4 displayed no such cracking and had a modest deposition depth. Single track depositions produced with an additional remelting step using the parameters 5 to 8 in Table 3.1 were observed to have extensive crack formation. This led to samples 5, 7, and 8 detaching from

the substrate shortly after production, see figure 4.4. A more detailed examination revealed that all these samples exhibited pronounced cracks at the interface between the substrate and deposit, see figure 4.5 (a), (e), (f), (g), (h). This observation raised the question of whether these cracks are formed due to a compositional mismatch between samples and substrate.

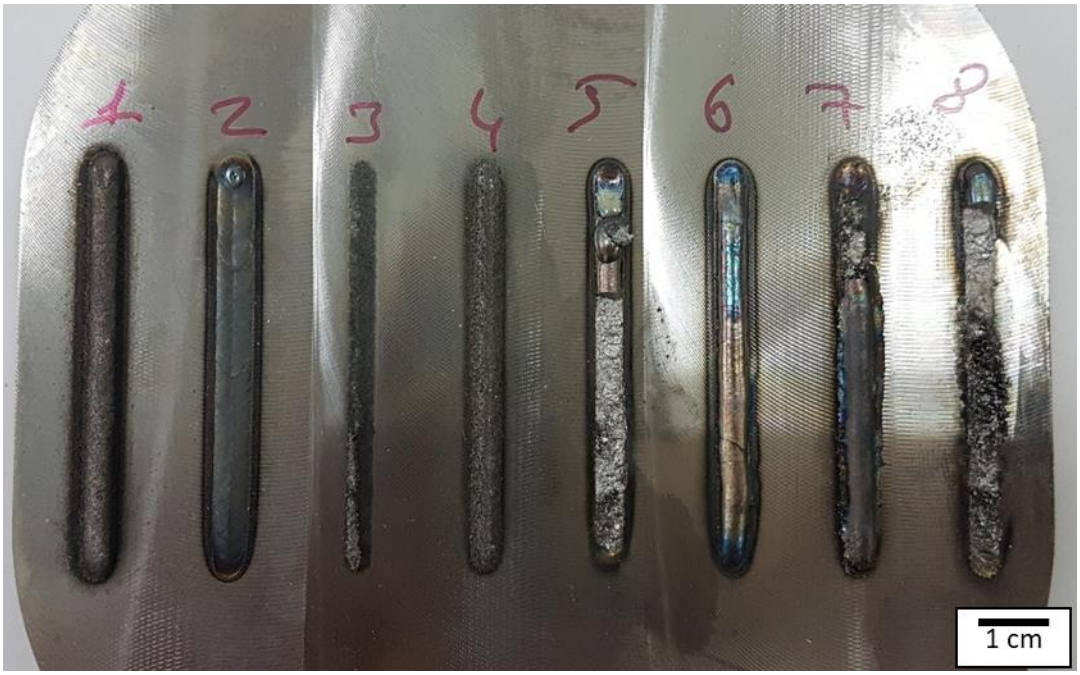

Figure 4.4. First batch production of samples 1 to 8.

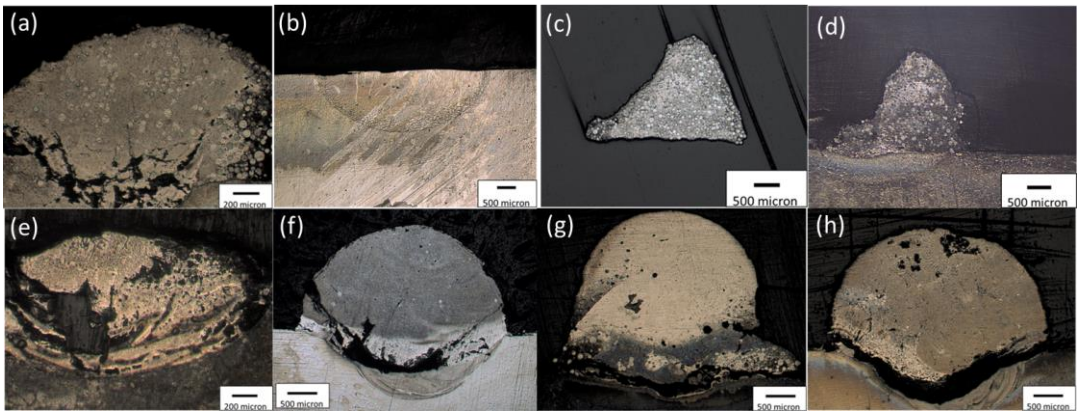

Figure 4.5. OM micrographs of (a) sample 1, (b) sample 2, (c) sample 3, (d) sample 4, (e) sample 5, (f) sample 6, (g) sample 7, and (h) sample 8.

Deposition behavior of singles tracks exhibited that parameters 1, 6, 7, and 8 were potential candidates for subsequent optimization studies. To delve deeper, XRD analysis was conducted on these samples. The results from this analysis showed that in addition to the unmolten Ta and Mo powders, there was a formation of Fe-Ta intermetallic phases in samples 1 and 6. In contrast, samples 7 and 8 did not exhibit any distinguishable intermetallic (IM) peaks, see figure 4.6.

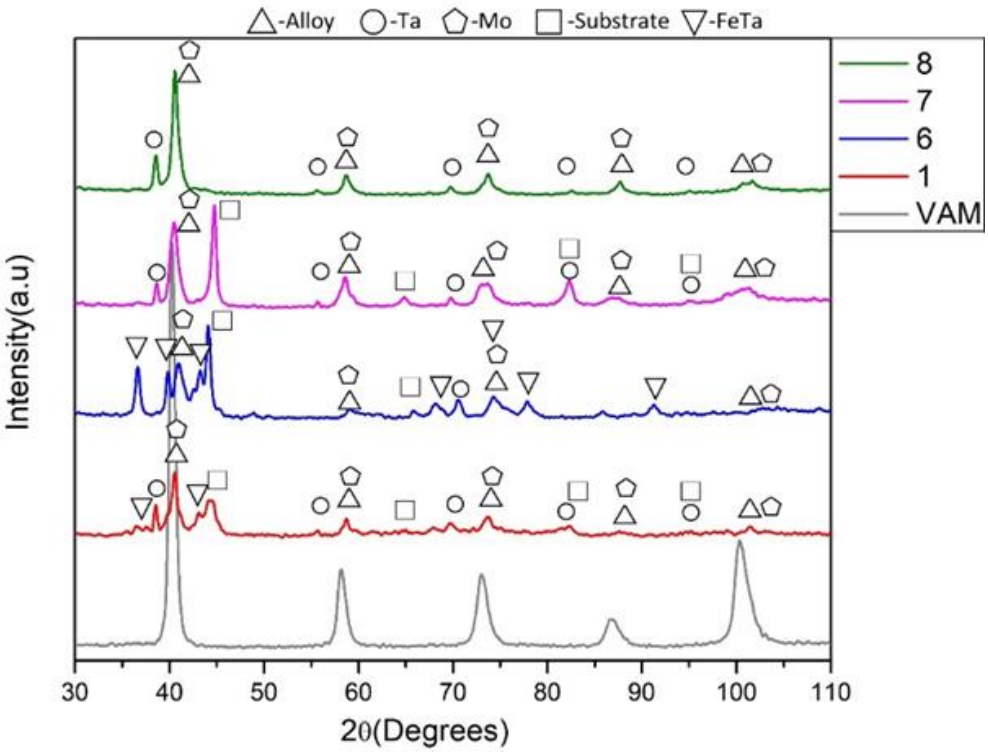

Figure 4.6. XRD analysis of samples 1, 6, 7, and 8 in comparison with VAM sample.

Subsequent SEM analyses were performed on samples 7 and 8, see Figure 4.7. Sample 7 revealed a substantial amount of unmolten powder, with clearly distinguishable layer borders. In contrast, sample 8 had fewer unmolten powders, and the deposition layers were indiscernible. These observations suggest that the parameters for sample 8 may be suitable candidates for second-batch production.

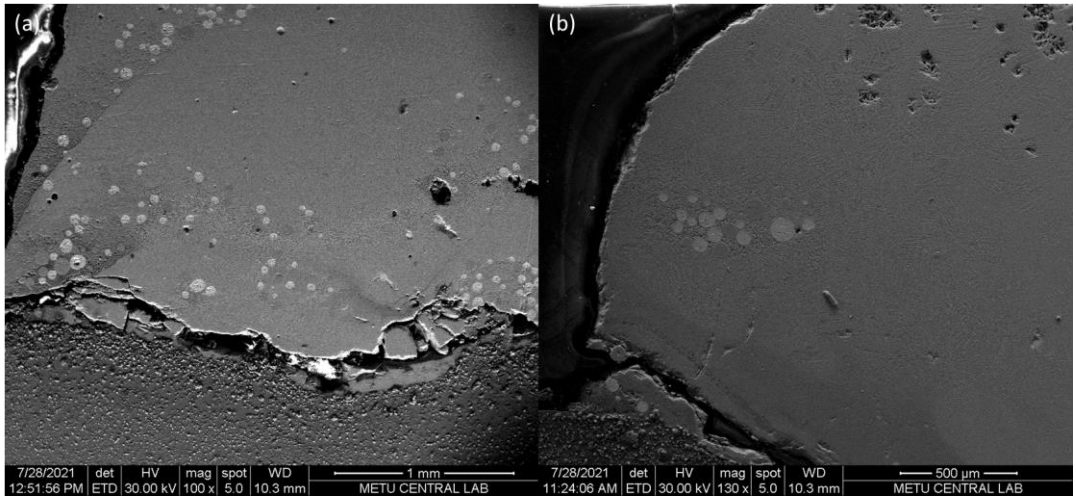

Figure 4.7. SEM images of (a) sample 7, and (b) sample 8.

4.3.1.2 Second batch production

Given the presence of unmolten powders in the initial batch, it was decided to implement second and third remelting steps for subsequent trials. In the second batch, thin-wall production was conducted to evaluate the potential for bulk manufacturing. Samples 9, 10, and 11 were produced based on the parameters from sample 8 but underwent 1, 2, and 3 remelting steps, respectively, see Table 3.2. Despite the relative success with the single-track productions, these parameters yield unsatisfactory outcomes, with notable issue unable to build consistent and sufficiently high walls due to excessive melting, see Figure 4.8. Moreover, EDX analysis revealed a significant evaporation of low melting alloying elements in the system, see Table 4.2. To address this issue, it is decided that to increase melting temperature of primary alloy formed at deposition step. Therefore, deposition laser power was decided to increase. Since in sample 1 there were sufficient deposition, it is decided to increase deposition power to 2000 W. also in-situ observations revealed that high remelting power results in excessive melting. Thus, remelting power is reduced to 2000 W. Consequently, samples 12, 13, and 14 were produced

successfully. For sample 12 and 13 laser power of 2000 W, deposition scan speed of 400 mm/min and remelting scan speed of 750 mm/min were used with number of remelting steps of 2 and 1, respectively. For sample 14 laser power of 2000 W, deposition scan speed of 500 mm/min and remelting scan speed of 1000 mm/min were used with 1 remelting step. All samples exhibited satisfactory builds, Figure 4.9 shows samples 12 and 13 with sufficient wall heights.

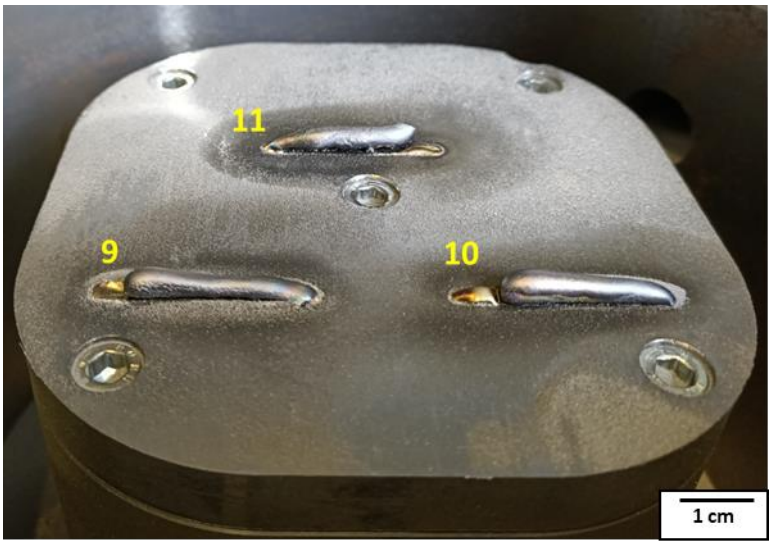

Figure 4.8. Thin wall production of samples 9, 10, and 11.

Table 4.2 EDX analysis of sample 10.

element	*Cr*	*Mo*	*Ta*	*Ti*	*V*
Amount in powder mixture (at%)	10 ± 0.1	25 ± 0.1	25 ± 0.1	15 ± 0.1	25 ± 0.1
Amount in produced sample (at%)	6.7 ± 0.3	24.9 ± 0.2	58.8 ± 0.7	5.2 ± 0.3	4.5 ± 0.3

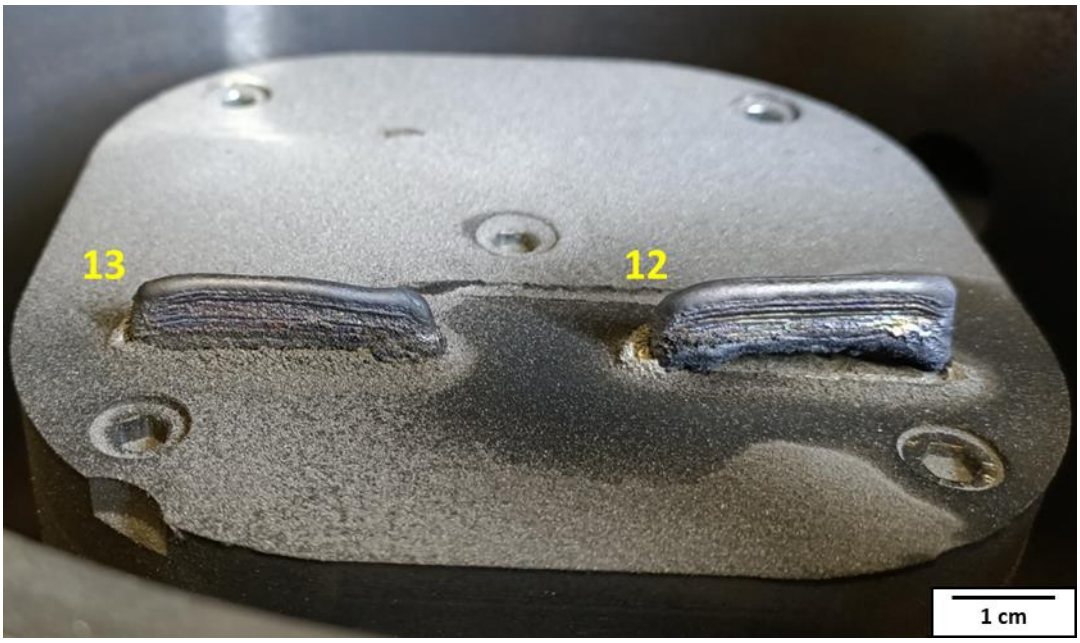

Figure 4.9. Thin wall production of samples 12 and 13.

Subsequent pore analysis on the samples indicated that sample 12 achieved the highest density, having a porosity of 0.37% ±0,13, see Table 4.3. Based on these results, the parameters for sample 12 were chosen for production.

Table 4.3 Pore analysis of samples 12, 13, and 14.

Sample	**12**	**13**	**14**
Pore (% area)	0.37 ± 0.13	0.62 ± 0.16	0.51 ± 0.19

4.3.2 Phase analysis

XRD analysis of these samples revealed the formation of a BCC phase, consistent with VAM-produced alloys, see Figure 4.10. However, while the XRD analyses from the bottom part of the samples which is close to the interface indicate the

presence of an Fe-Ta IM phase, upper part has only a single-phase BCC structure. Therefore, all further analyses were conducted at the regions away from the interface between deposition and the substrate.

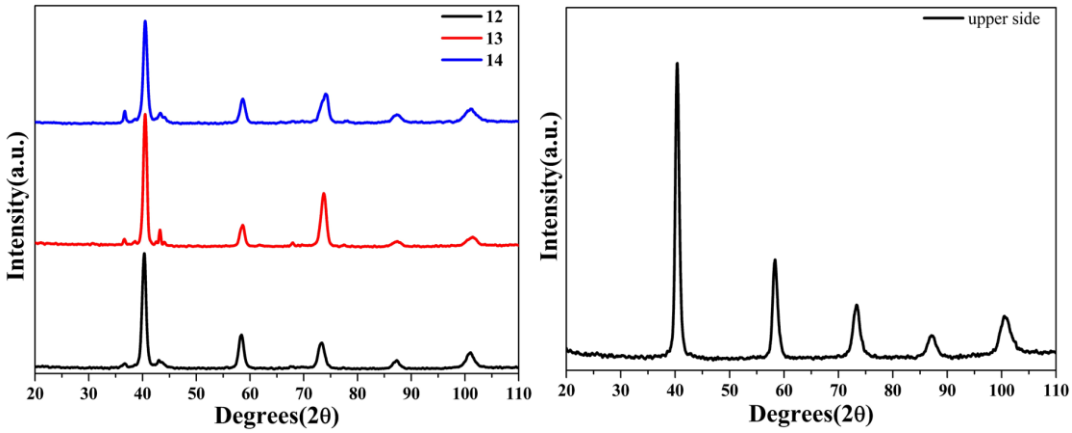

Figure 4.10. XRD diffractogram of samples 12, 13, 14, and the upper side of sample 12.

4.3.3 Microstructure

OM results revealed a dendritic structure formed during production, similar to that observed in VAM-produced samples. Interestingly, unlike VAM-produced samples the dendrite size remained consistent throughout the DED-produced sample, see Figure 4.11. This difference shows during DED production solidification occurs with uniform thermal gradient, resulting in uniform dendrite size distribution. Moreover, direction of dendrites in DED sample shows there is no preferred direction these dendrites are formed. This random distribution of dendrites indicates an isomorphous structure is achieved. The isomorphous nature of the dendritic structure further suggests that there isn't a preferred orientation during solidification.

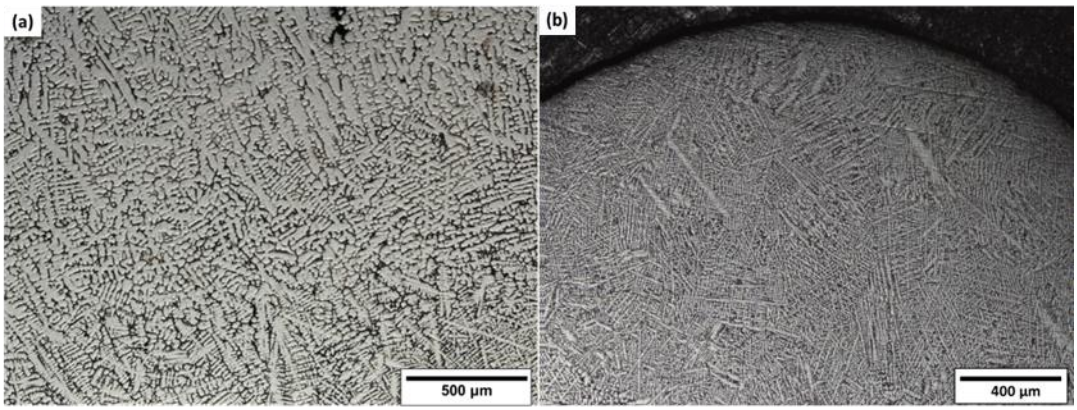

Figure 4.11. Dendritic structures of (a) VAM-produced sample, and (b) DED-produced sample.

Crack formation at the substrate deposit interface has been observed in all produced samples. This crack formation leads to easy detachment of samples after production. Moreover, extensive cracking observed on single-track productions indicates a high residual stress accumulation. This occurs due to repeated rapid heating and cooling of deposited layers [108–111]. However, this extensive cracking did not observe in thin walls. Even though energy density was higher in thin wall production, cooling rates were reduced with each deposited layer. Therefore, stress accumulation was reduced with each subsequent layer.

4.4 Effect of production method on Cr10Mo25Ta25Ti15V25 RHEA

4.4.1 EDX analysis

Figure 4.12a shows the elemental distribution in VAM produced Cr10Mo25Ta25Ti15V25 alloy. There is some V, Ti and Cr segregation while Ta and Mo depletion occurs at the interdendritic regions. Similarly, Figure 4.12b shows segregation/depletion behavior of the alloy under non-equilibrium cooling conditions calculated by CALPHAD method. Scheil cooling diagram in Figure 4.12b

indicates that Ti and Cr have a high tendency to be saturated in the liquid during solidification. This occurs due to their relatively low melting temperatures. Another low melting temperature element, V, initially exhibits large enrichment in the liquid at high temperatures and then enrichment amount decreases below ~1750 °C. This diagram also suggests that Mo and Ta solidify more easily than other elements in the system due to their high melting temperatures which results in the precipitation of Ti, Cr and V at the interdendritic regions and saturation of dendritic regions by Ta and Mo[112]. Clearly, Scheil calculations match well with the segregation behavior of the elements observed by EDX analysis.

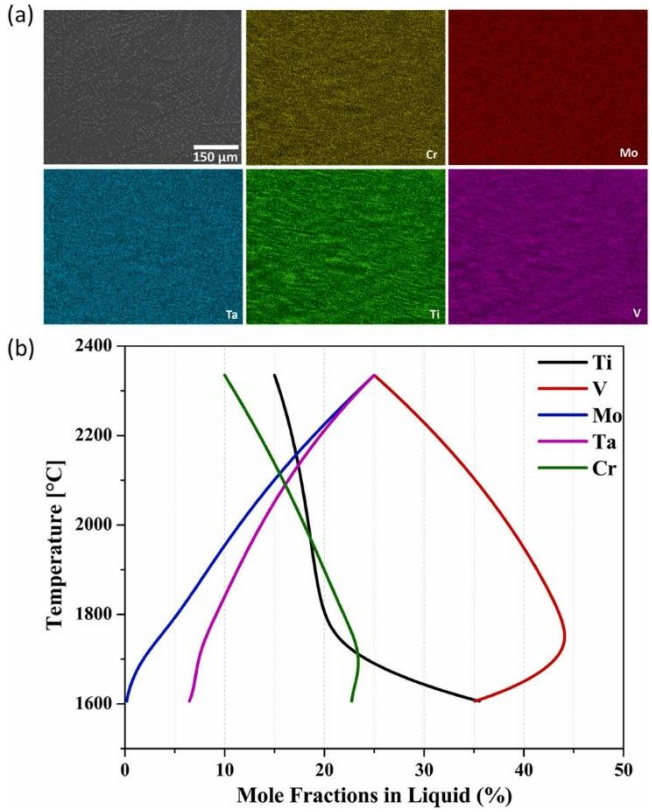

Figure 4.12. (a) EDX mapping showing the elemental distribution in Cr10Mo25Ta25Ti15V25 alloy, and (b) T vs. mole fraction in liquid under non-equilibrium (Scheil) condition showing segregation/depletion behavior of individual elements.

Initial analysis on DED samples revealed Fe-Ta IM formation at the bottom of the samples. Although XRD analysis of upper parts did not indicate any IM formation. However conventional XRD detectors are not able to detect small fractions of any phase due to their low sensitivity. Therefore, Fe also added to the Z-list to determine any saturation in the microstructure. EDX analysis on DED samples showed there was ~2 at% Fe even at the upper parts of the wall, revealed from the EDX maps in Figure 4.13. However, Fe distribution was homogenous throughout the sample. this indicated Fe-Ta intermetallic phase did not form upper part of the sample. It is known that increased energy density in remelting has the potential to increase diffusion from the substrate[94]. Although IM formation was limited to lower layers, Fe diffusion remained an unresolved issue for this alloy. Even though IM formation can be avoided by using different substrate materials, preferably one made from constituting elements, many studies showed that diffusion of substrate material is unavoidable[92,94,113]. Moreover, elemental partitioning observed in VAM samples also observed in DED samples. On the other hand, along with saturation of interdendritic regions Ti map showed accumulation of this element. This suggested possible secondary Ti-rich phase particle formation in the system.

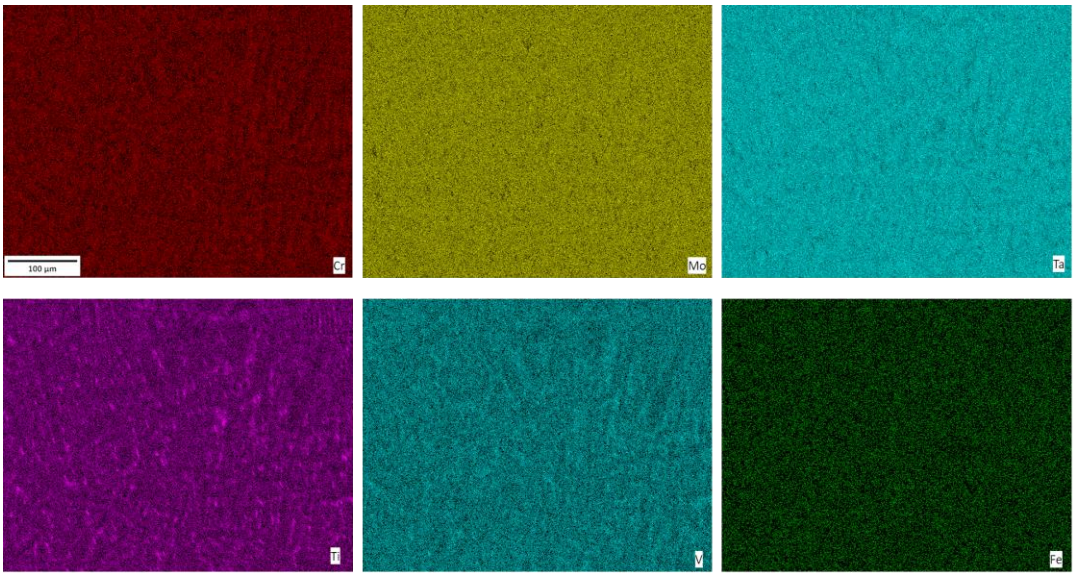

Figure 4.13. EDX mapping showing elemental distribution at the upper part of the RHEA.

4.4.2 EBSD analysis

Figure 4.14 shows the EBSD analysis on VAM produced Cr10Mo25Ta25Ti15V25 alloy. Grains in Figure 4.14a seem to have random orientations, inferring random nucleation and growth in the system[114]. Moreover, there are some equiaxed grains formed within and between the dendritic structure. KAM map in Figure 4.14b showing the strain distribution indicates that the strain level in the microstructure is not homogenous. In other words, the regions where nanocrystals exist are in a high strain state while some regions have low dislocation density. Besides, the boundaries are found to be mostly high angle grain boundaries, as seen in Figure 4.14c. When a smaller region with high precision is scanned, some of the fine features can be captured (Figure 4.14d). It can be clearly seen that there are very fine grains bonded by high angle grain boundaries. However, most of these grains are in nano-scale, requiring further investigation using TEM.

Subsequent EBSD analysis of the DED sample highlighted a relatively large grain structure with an average of 102 ± 3 µm (Figure 4.15a). According to the orientation map, a small number of elongated grains is detected. Moreover, the orientation map in Figure 4.1.a indicates a slight dominance of blue color which corresponds to the grains aligned in the built direction, which is a typical phenomenon for the additively manufactured dendritic structures[115]. Although, pole figures and IPFs given in Figure 4.15b and Figure 4.15c indicate a slight growth along the building direction (100), no dominant grain growth along building direction is observed. Also, by considering almost equal grain densities in (100), (110), and (111) directions in pole figures given in Figure 4.15b, no significant texture is observed.

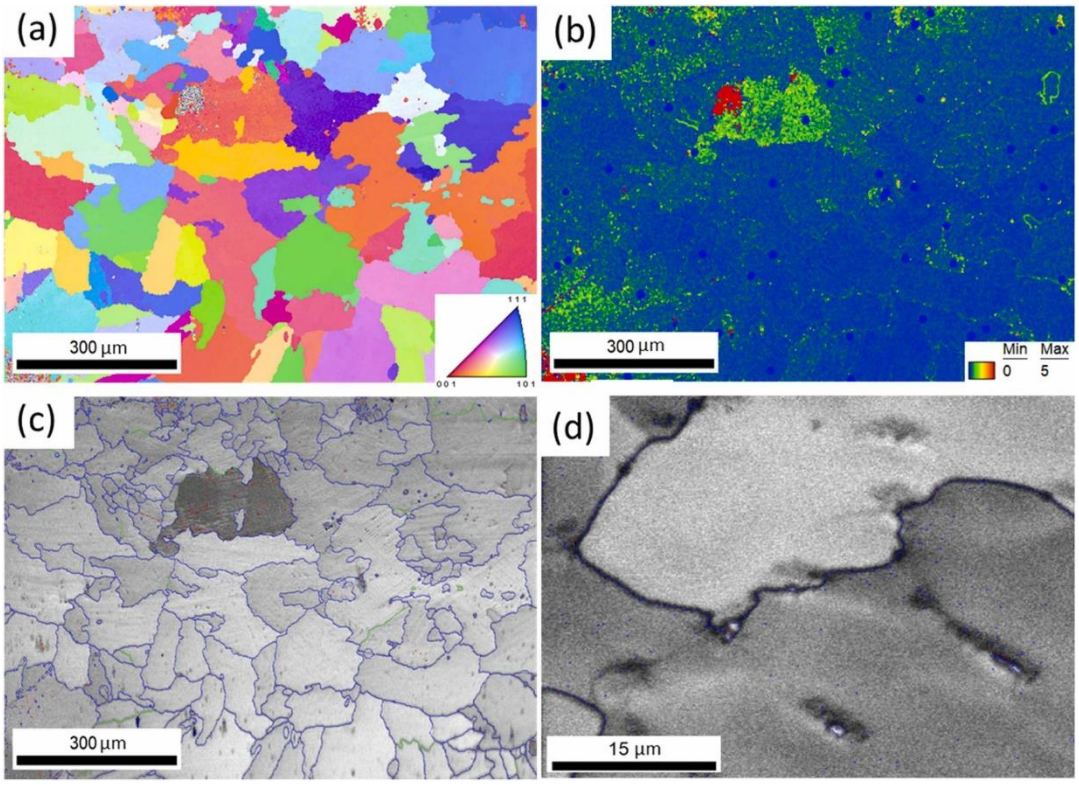

Figure 4.14. (a) EBSD orientation map, (b) kernel average misorientation map, (c) grain boundary misorientation map, and (d) grain boundary misorientation map at high magnification showing submicron size grains with high angle grain boundaries. In (c) and (d), blue, green and red colors correspond to high angle grain boundaries

(> 15°), low angle grain boundaries between 15°− 5° and low angle grain boundaries between 5°− 2°, respectively.

Additive manufactured RHEAs often have complex microstructures due to complex temperature histories between each deposition layer. Dobbelstein et al. [92] showed that different cooling rates in each layer affect average grain size along the build direction. In a recent study, Gou et al.[116] identified the grain morphology's dependence on the G/R value, where G represents the temperature gradient at the solid-liquid interface, and R denotes the solidification velocity [117]. A high G/R value typically leads to columnar grain growth, while a lower value produces equiaxed grains[116,118]. DED production did not result in entirely equiaxed grains but commendably avoided columnar grain formation. This implies the attainment of a high-temperature gradient at the solid-liquid interface, leading to a microstructure devoid of any specific texture. Such a texture-free microstructure indicates that the produced samples are likely isomorphous structures.

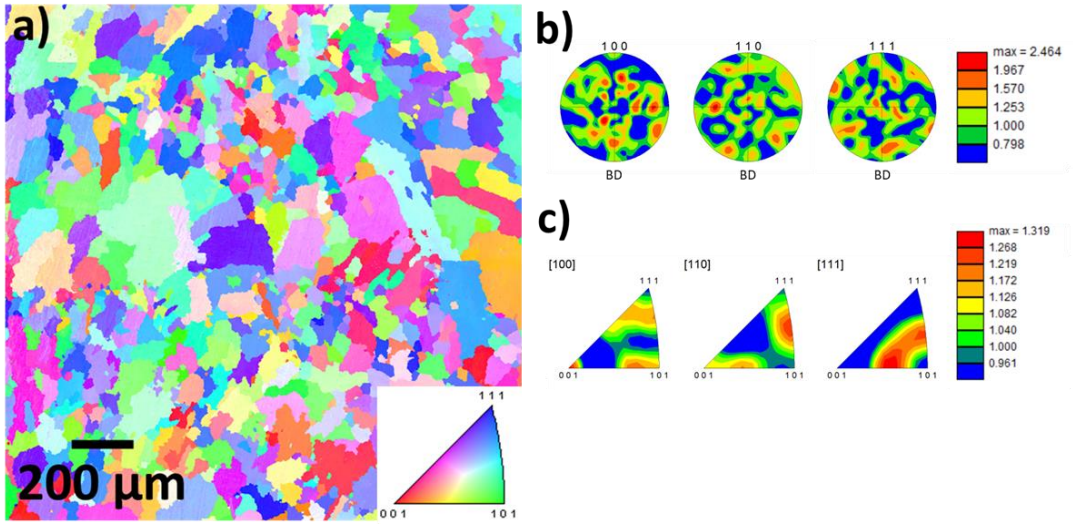

Figure 4.15. a) EBSD orientation map, b) pole figures, and c) inverse pole figures.

4.4.3 TEM analysis

Detailed TEM analysis was conducted on VAM samples. Similar to the EBSD observations, TEM analyses revealed the presence of submicron grains and cells within the large dendrites. As shown in Figure 4.16a, many submicron grains with high angle grain boundaries can be observed, suggesting they are the same submicron-crystallites with high angle boundaries depicted in Figure 4.14d. In addition to these, the presence of sub-grains bounded by dislocations is observed. Figure 4.16b further depicts the submicron crystallite regions where grain boundaries are primarily formed of dislocations and dislocation loops. It has been reported that fast cooling rates promote the formation of dislocation cells[119,120]. Consistent with this, the small sample sizes used for microstructural analyses in this study meant a fast-cooling rate, resulting in both dislocation cells and various other dislocation structures.

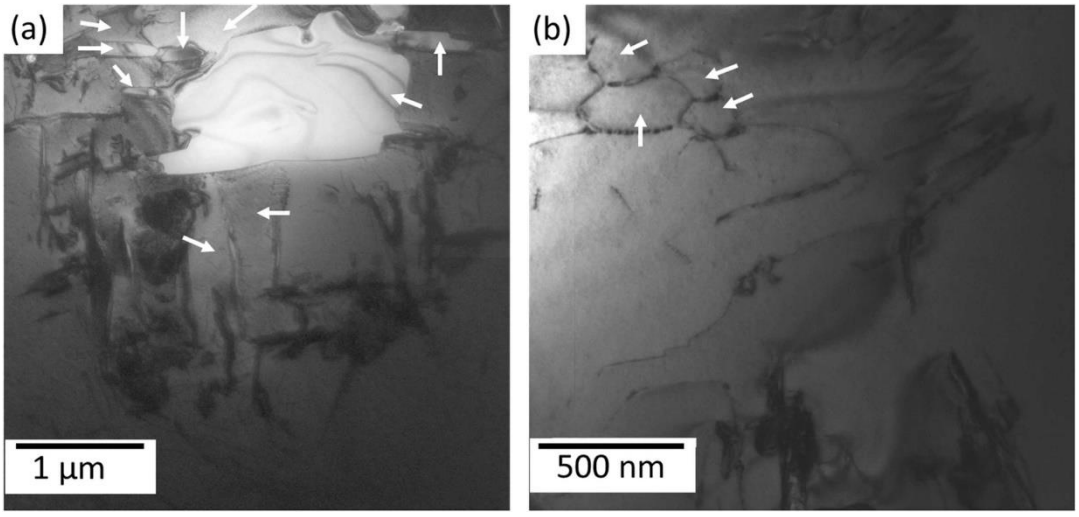

Figure 4.16. BFTEM images of submicron crystallite regions having (a) mostly high angle boundaries, and (b) dislocation boundaries. White arrows point the submicron crystalline regions.

Different dislocation structures have been observed in this alloy. Two-beam imaging studies have been performed along g < 110 > and g < 200 > by tilting from [001] zone axis. Figure 4.17a and b show dislocation tangles besides linear dislocations. Figure 4.17c shows linearly aligned dislocation loop structures, similar to the ones observed in EBSD analyses (Figure 4.14d). However, their size is less than 50 nm; thus, the small aligned features that cannot be well distinguished in EBSD are presumed to be the dislocation loops. Wang et al.[121] have reported the dislocation debris (e.g., loops, jogs, dipoles) after 10 % tensile deformation in nitrogen-doped TiZrNbTa high entropy alloys. Similarly, Wu et al.[122] [44] observed dislocation debris in a VNbTi medium entropy alloy after deformation. It has been reported that they result from cross slip and multiplanar slip of screw dislocations after decomposition of jogs and dislocation forests[121,122]. In this study, rapid cooling rates due to small size of the samples result in such dislocation structures due to significant supersaturation of the vacancies[123].

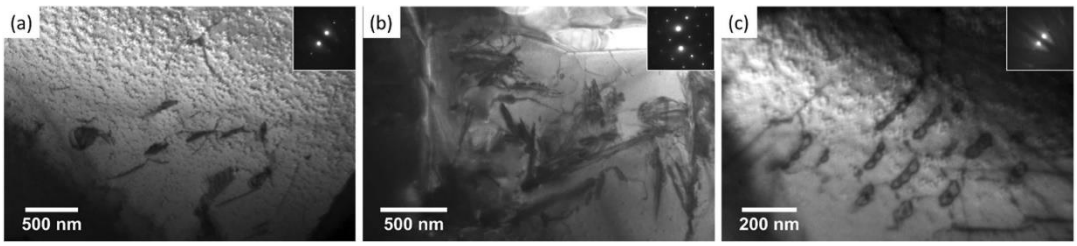

Figure 4.17. Dislocation structures showing (a, b) dark regions of tangles and dislocation networks, and (c) linearly aligned loops. BFTEM images in (a) and (c) were taken along g < 110 > while (b) was taken along g < 002 >.

In the regions where a strong diffraction contrast is observed in BFTEM, detailed analyses have been conducted. Figure 4.18a shows the existence of submicron-grains as well as a secondary phase when the large grain in the background is tilted to [001] zone axis. The diffraction spots encircled by red color belong to BCC RHEA while planes labeled in white color belong to Ti-rich second phase having FCC crystal

structure along [110] zone axis. The lattice parameter of this phase has been calculated as 4.42 Å. High annular angular dark field (HAADF) image in Figure 4.18b clearly shows the concentration difference in bright and dark grains (and needle-like features) in Figure 4.18a. Darker grains have smaller weights compared to the background RHEA composition. EDX analysis also indicated that these regions are rich in titanium with some carbon, which is the solid solution of Ti-C having FCC crystal structure. Here, carbon comes from either the raw materials or VAM chamber contamination. Moreover, TEM analysis on DED samples was conducted to analyze Ti-rich clusters observed in EDX maps. This analysis validated Ti-rich particle formation observed in EDX maps. Figure 4.19a and b shows TEM BF images of Ti-rich particles as bright particles. However, unlike VAM produced samples these particles contained O instead of C. This, oxygen inclusion can be explained by oxygen level during production. Although chamber constantly purged with Ar remaining O in the chamber was able to diffuse into the samples to form these Ti-rich particles. These results show that the Ti-rich particles act as solvents for impurities, which are a byproduct of the production techniques used in this study.

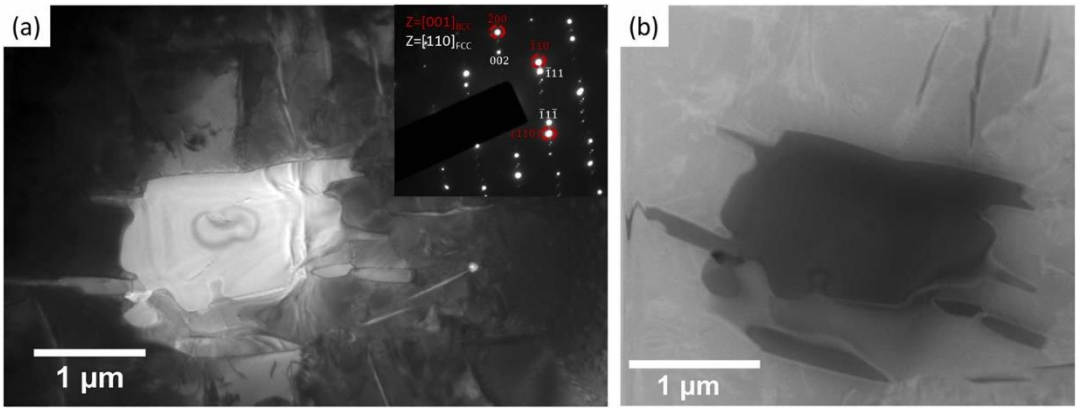

Figure 4.18. (a) BFTEM image showing the nano-crystalline region along the BCC zone axis of [001], and (b) HAADF image at this region showing different compositions in some of the nano-grains compared to the matrix. Inset in (a) shows the SAED pattern labeled by red (BCC-RHEA) and white (FCC-Ti) color.

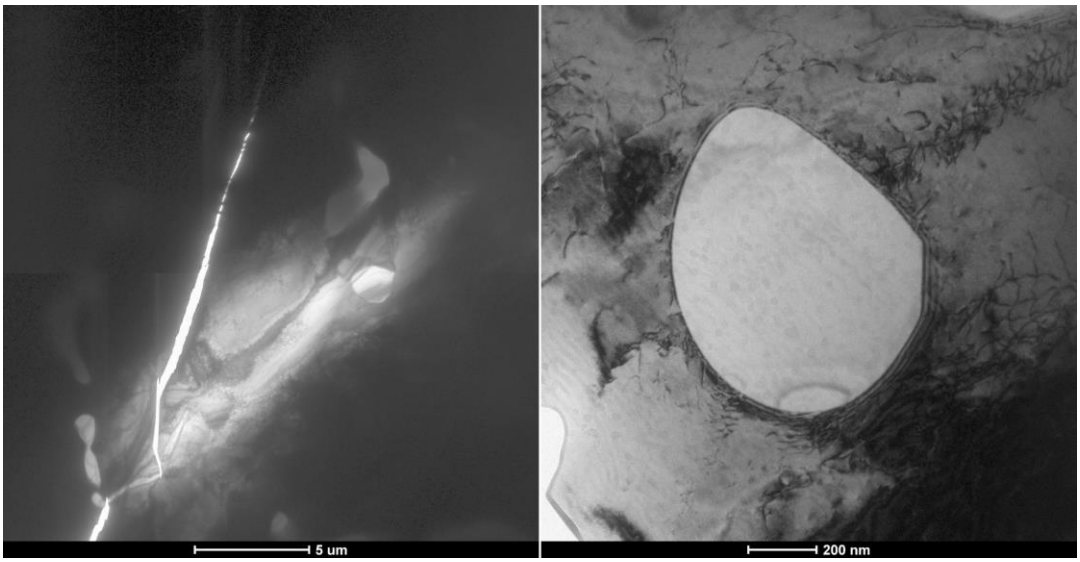

Figure 4.19. Ti rich-FCC particles.

Recently, nano-scale FCC-Ti formation has been reported in either deformed or high temperature heat treated/sintered alloys[124–128]. For instance, Jiang et al.[124] reported the formation of FCC- Ti (Ti-C solid solution) phase in a Ti37Nb28Mo28–C7 alloy hot pressing sintered at 1300 °C as a result of rearrangement of atoms mediated by interstitial carbon atoms by creating energy variations in the lattice. Similarly, Li et al.[129] observed FCC-Ti formation in TiNbMo0.5Alx alloys, which are produced by vacuum arc melting, as a result of Al atoms creating energy variations in the lattice. On the other hand, Chang et al.[130] have shown that TiHx forming either during electropolishing or FIB preparation has also FCC crystal structure with similar needle-like morphology and lattice parameter. In this study, together with needle-like particles, equiaxed and slightly elongated phases can be observed. Besides, even though no information is available on hydrogen which cannot be detected by EDX, EDX analysis indicates the existence of carbon or oxygen in this phase, depending on production method. Therefore, most of these particles/phases are determined to be FCC Ti-C and FCC Ti-O solid solution phase for VAM samples and DED samples, respectively. It should be noted that the concentration of the second phase is low enough not to appear in XRD analyses.

Li et al.[129] have studied the orientation relationship and coherency of FCC-Ti phase with BCC matrix and found that there is Kurdjumov-Sachs (K–S) orientation relationship between FCC and BCC along $\{111\}_{FCC}//\{110\}_{BCC}$ with coherency. However, in the present study, the interplanar distance mismatch is large, resulting in a disruption in orientation relationship and incoherency between the matrix and FCC-Ti phase.

EDX analyses have been conducted on the regions of dislocation tangles observed on VAM samples, seen as dark under BFTEM imaging conditions. Figure 4.20 shows the elemental distribution at a region having high dislocation density with entanglements. Clearly, these regions show different contrast under HAADF indicating a compositional variation. However, a completely random distribution of the elements can be seen in these regions. This confirms that the dislocation structures in Figure 4.17 are not entangled around a second phase.

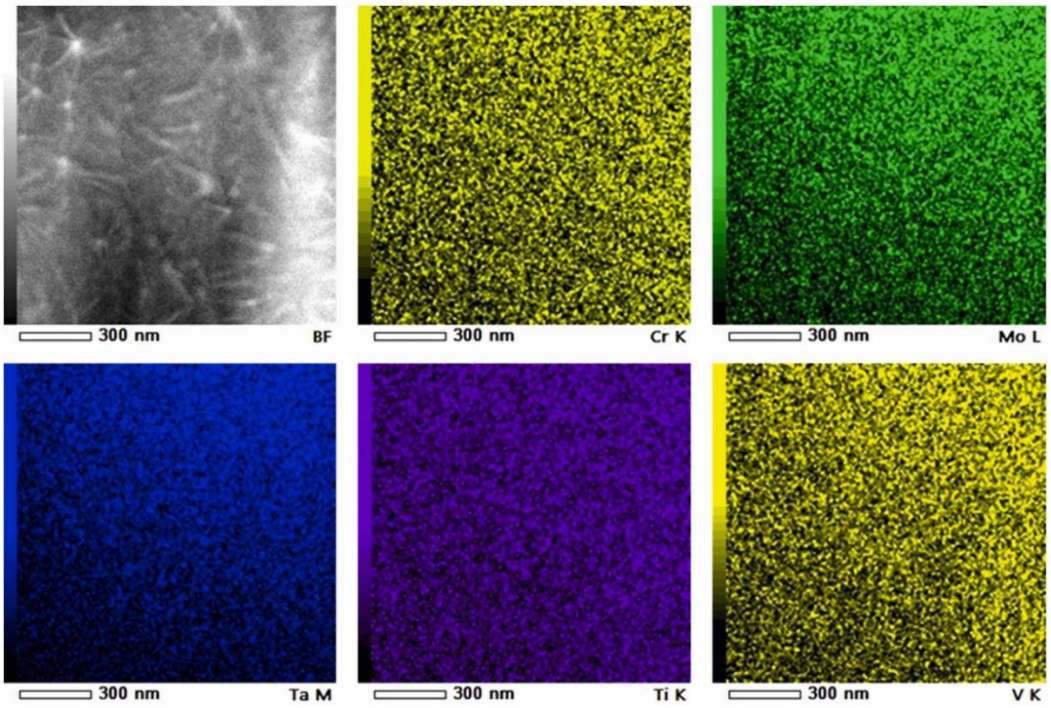

Figure 4.20. EDX maps at the heavily dislocated regions, showing a random distribution of the elements.

4.4.4 Compression tests

The mechanical behavior of this alloy has also been investigated in this study. For this purpose, compression tests were conducted at room temperature, 800 and 1000 °C.

4.4.4.1 RT tests

Compressive stress-strain curves of VAM sample in Figure 4.21 exhibit that the yield strength of this alloy is 1575 ± 10 MPa with 13 ± 2 %. on the other hand, room temperature (RT) tests on DED samples reported a yield strength of 1611 ± 30 MPa accompanied with 9 ± 1 % ductility. This suggests that the alloys produced using DED demonstrate superior strength when compared to those produced through VAM. However, this heightened strength is met with a decrease in ductility. According to the literature compiled by Miracle et al.[8] most of the RHEAs with VEC values higher than 5 show compressive strain lower than 5 %. Although its ductility seems to be low compared to the conventional alloys, Cr10Mo25Ta25Ti15V25 alloy shows substantially good strength / ductility combination with respect to other RHEAs with similar VEC values. Besides, it exhibits good strain hardening behavior.

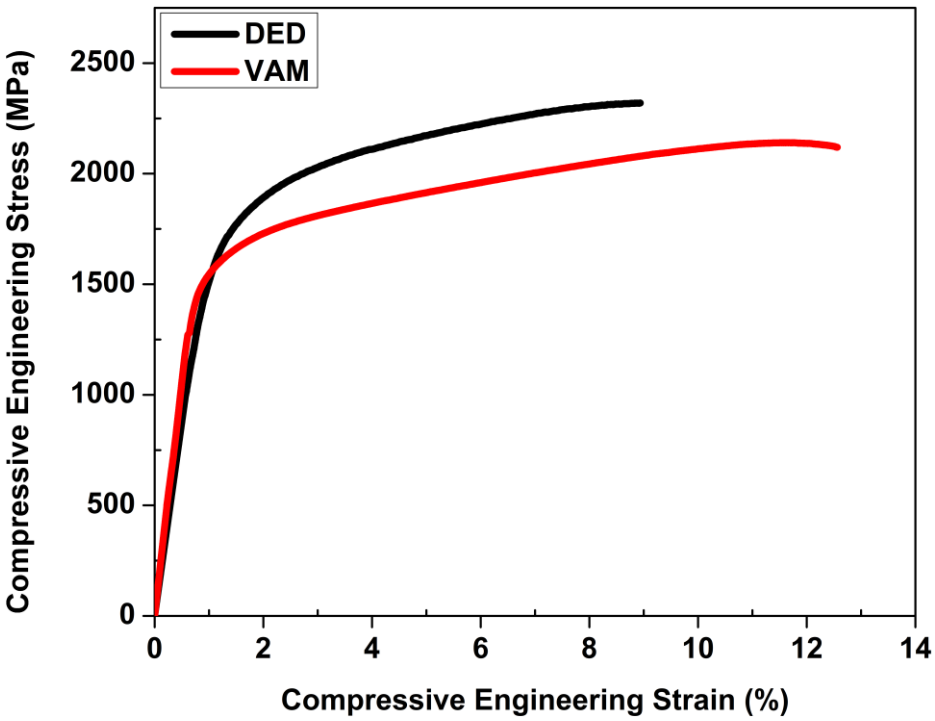

Figure 4.21. Compressive stress-strain curves of VAM and DED samples at RT.

Cr10Mo25Ta25Ti15V25 alloy in as-cast condition has some complex dislocation structures, such as loops, entangles, networks as well as a small amount of submicron crystallite FCC-Ti phase. In general, interfaces in dual phase alloys act as heterogeneous dislocation sources to provoke plastic deformation at the beginning of the deformation[131]. Besides, dual phase hetero-structure alloys which are composed of soft and hard phases with large grains and nano-crystallites are reported to be beneficial for improving strength and ductility[132–134]. In addition to that, the FCC-Ti exhibits extraordinarily high Young's modulus and compressive strength resulting in a high strength alloy [124]. Thus, high strength and ductility have been attributed to the deformation mechanisms and strain hardening ability of the alloys.

4.4.4.2 800 °C tests

To investigate the high temperature mechanical properties, VAM and DED samples has been tested at 800 and 1000 °C. Figure 4.22 shows that strength with increasing testing temperature for both production methods. For VAM samples strength decreases to 940 ± 40 MPa and for DED samples strength decreases to 1100 ± 50 MPa at 800 °C. This is attributed to thermal softening[45] . Besides, VAM samples showed a slight decrease in ductility of the alloy. FCC Ti has been reported to be promoted by plastic deformation and annealing[125,135]. Thus, the fraction of FCC phase might have increased as a result of deformation at 800 °C which introduces increased amount of BCC/FCC boundary pinning effect[129]. However, even though FCC Ti also observed in DED samples, there were no observed decrease in ductility. Therefore, effect of FCC Ti phase on plasticity has to be confirmed with further experiments.

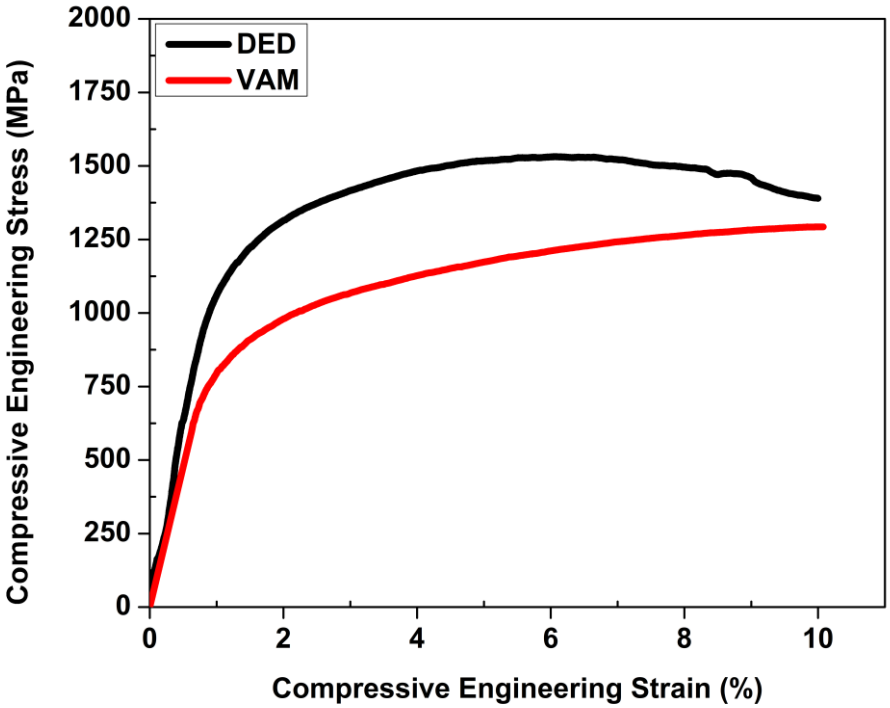

Figure 4.22. Compressive stress-strain curves of VAM and DED samples at 800 °C.

4.4.4.3 1000 °C tests

At a higher temperature of 1000°C, the VAM samples presented a yield strength 640 ± 50 MPa and DED samples showed 953 ± 70 MPa, see Figure 4.23a. Along with thermal softening dynamic recovery and recrystallization was observed in VAM samples[45] . this can be observed from the small strength increase from YS to UTS. On the other hand, DED samples showed an impressive over 45 % ductility without fracture. At this temperature, steady state flow was achieved up to 30% strain. however due to low height of the initial samples, compensation of area increase was not possible. Therefore, dead metal zone formation and increase in stress was observed. Figure 4.24(a), (b), (c), and (d) shows DED compression test samples as-prepared, after RT, 800 and 1000 °C tests, respectively. Figure 4.23b compares the compressive yield strengths of various RHEA systems with this study[6,43,45–49]. Clearly, CrMoTaTiV alloy has high yield strength at RT and retains its high strength at higher temperatures up to 1000 °C regardless of production method.

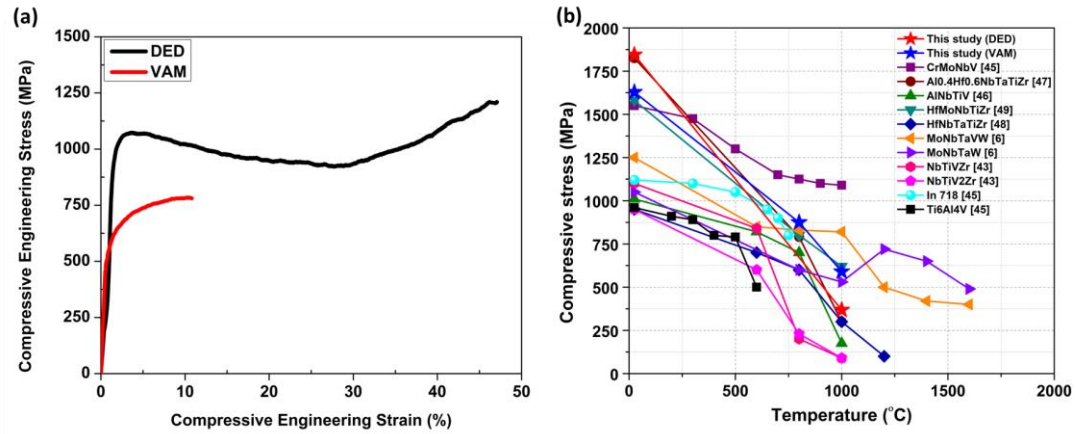

Figure 4.23. (a) Compressive stress-strain curves of VAM and DED samples at 1000 °C, and (b) comparison of yield strength of this study with the literature [6,43,45–49].

The exceptional strength of CrMoTaTiV RHEAs can be attributed to the intense lattice distortion resulting from various elements randomly occupying lattice

positions[3]. This distortion hinders the dislocation slip, thereby increasing the shear stress and revealing the high-yield stress characteristic of RHEAs[3,41]. Furthermore, the presence of Mo, known for forming strong Mo-M bonds, adds to this strength[136–138]. Notably, the composition obtained from DED method contains a higher Mo content compared to VAM-produced samples, leading to enhanced strength.

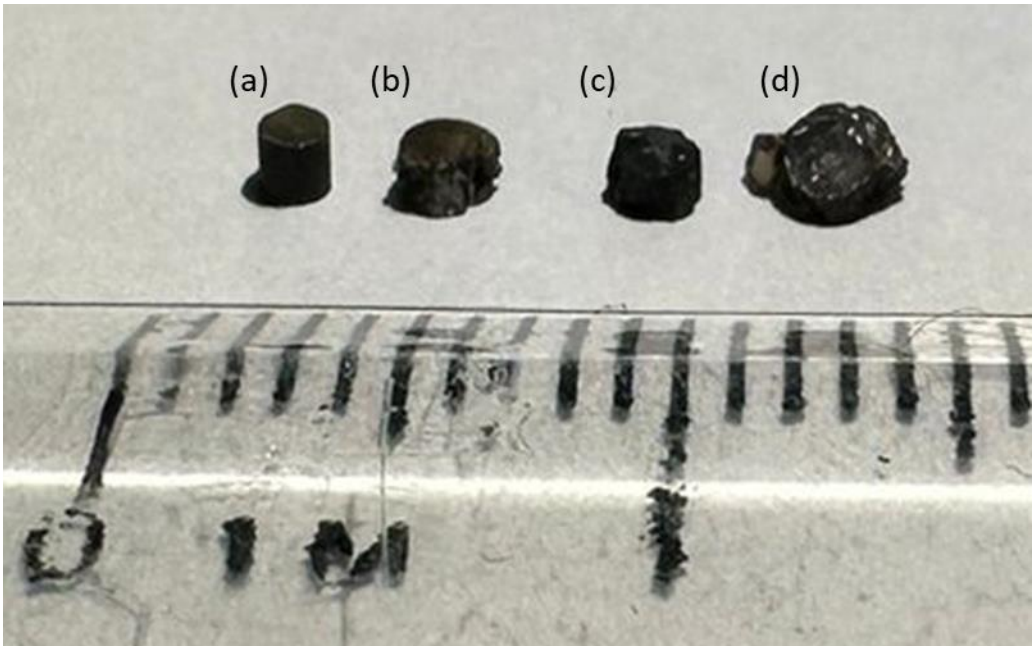

Figure 4.24. Compression test samples (a) as-prepared , (b) after RT test, (c) after 800 °C test, and (d) after 1000 °C test.

The texture-free microstructure of the sample's hints at their probable isomorphous nature, suggesting potential isotropic behavior. This means it can be anticipated consistent mechanical behavior in samples regardless of their orientation. Such isotropy is a significant advantage for additively manufactured samples[115,116]. This material can be employed in various applications without being constrained by the building direction, broadening its production capabilities.

CHAPTER 5

CONCLUSION

In this research, the Cr10Mo25Ta25Ti15V25 Refractory High Entropy Alloy (RHEA) was successfully developed and the effects of different production methodologies were systematically analyzed. The primary goal was to design a novel RHEA with notable attributes: significant ductility under compression (over 10%), moderate density (less than 10 g/cm^3), and remarkable high-temperature stability.

To achieve this, computational method which employs a dual strategy combining empirical calculations and CALPHAD studies were used. The empirical approach considers the parameters such as enthalpy, entropy, omega, atomic size difference, Pauling electronegativity, and valence electron concentration to evaluate the alloy's potential to form solid solution. A key requirement was to prevent the formation of intermetallic phases (IM), given their inherent brittleness. CALPHAD studies, conducted with the Thermo-Calc software and TCHEA6 database, provided further insights into possible phase formations.

The first part of the study emphasized the development and production of the Cr10Mo25Ta25Ti15V25 RHEA through the Vacuum Arc Melting (VAM) technique. Using XRD analysis, the formation of a single BCC phase was confirmed, consistent with established literature. Further characterization studies were also conducted on VAM-produced samples. SEM analysis showed that there was a segregation between dendritic and interdendritic regions. CALPHAD studies on the solidification behavior of constituting elements under fast cooling conditions showed similar results due to the different melting temperatures of these elements. As a result, depletion of Ta and Mo observed in interdendritic regions. Detailed TEM studies revealed the existence of dislocation tangles, loops, and networks as a result of planar slip and cross-slip of screw dislocations and the formation of a Ti-rich FCC

phase. Besides this FCC phase, a secondary BCC phase formation was observed depending on heat treatment time at low temperatures. Moreover, this RHEA did not show any HCP phase formation which can induce brittleness in the material. This RHEA showed high strength reaching 1575 MPa and noteworthy ductility at roughly 14%. This high strength is attributed to the dislocation tangles and high strength Ti-rich phase. While the alloy showed high strength and good strain hardening ability at room temperature, these properties of the RHEA decreased at elevated temperatures due to thermal softening. However, it still exhibited relatively high strength values even when tested at 1000°C in comparison to other RHEAs.

In the second part of this study, focus was to produce the novel Cr10Mo25Ta25Ti15V25 RHEA through in-situ alloying of pre-mixed powders via Directed Energy Deposition (DED) method. Two different parameter sets, leading to different final build forms, were used for parameter optimization. The first set was for generating three-layer, single-track samples, which were assessed using OM, SEM, and XRD techniques. OM and SEM confirmed that complete homogenization without a remelting step was not achievable for this RHEA, due to the unmolten Ta and Mo powders. The XRD assessments indicated that the chosen Fe substrate was highly diffusive in the RHEA, with the emergence of a Ta-Fe intermetallic compound during the process. For the second parameter set, it was aimed at creating thin-walled samples. Preliminary analysis using OM, SEM, and XRD demonstrated that the samples were fully homogenized. Additionally, the XRD examination of the walls indicated Ta-Fe intermetallic formation was restricted to layers adjacent to the substrate. Once the first half of the build was complete, Fe diffusion wasn't sufficient for any intermetallic phases. Further TEM analysis found the existence of FCC-Ti, but unlike the VAM-produced alloy, this phase in the DED samples contained O rather than C. This indicates the alloy's ability to accommodate impurities up to a certain threshold by developing the FCC-Ti phase and accommodating the inclusions within. There was an enhancement in mechanical properties due to the compositional change during DED. Tests at room temperature (RT), 800°C, and 1000°C displayed strength improvement at all tested temperatures. While there was reduced ductility

at RT and 800°C, the alloy displayed superior ductility at 1000°C when compared to the VAM-produced samples.

In essence, this study illuminated the potential of the Cr10Mo25Ta25Ti15V25 RHEA, showing its unique characteristics and adaptability across different production methods.

REFERENCES

1. Huang, P. K., Yeh, J. W., Shun, T. T. & Chen, S. K. Multi-principal-element alloys with improved oxidation and wear resistance for thermal spray coating. *Adv Eng Mater* **6**, 74–78 (2004).

2. Cantor, B., Chang, I. T. H., Knight, P. & Vincent, A. J. B. Microstructural development in equiatomic multicomponent alloys. *Materials Science and Engineering A* **375–377**, 213–218 (2004).

3. Gao, M. C., Liaw, P. K., Yeh, J. W. & Zhang, Y. *High-Entropy Alloys*. *High-Entropy Alloys: Fundamentals and Applications* (Springer International Publishing, 2016). doi:10.1007/978-3-319-27013-5.

4. Yeh, J.-W. *et al.* Nanostructured High-Entropy Alloys with Multiple Principal Elements: Novel Alloy Design Concepts and Outcomes. *Adv Eng Mater* **6**, 299–303 (2004).

5. Scripta Materialia Cr-Mo-V-W A new refractory and transition metal high-entropy alloy system ☆ - Ikeuchi et al. - Unknown - 2019.pdf - U.pdf.

6. Senkov, O. N., Wilks, G. B., Scott, J. M. & Miracle, D. B. Mechanical properties of Nb 25Mo25Ta25W25 and V20Nb20Mo20Ta20W20 refractory high entropy alloys. *Intermetallics (Barking)* **19**, 698–706 (2011).

7. Senkov, O. N., Wilks, G. B., Miracle, D. B., Chuang, C. P. & Liaw, P. K. Refractory high-entropy alloys. *Intermetallics (Barking)* **18**, 1758–1765 (2010).

8. Miracle, D. B. & Senkov, O. N. A critical review of high entropy alloys and related concepts. *Acta Mater* **122**, 448–511 (2017).

9. Wei, Q. *et al.* High-temperature ultra-strength of dual-phase Re0.5MoNbW(TaC)0.5 high-entropy alloy matrix composite. *J Mater Sci Technol* **84**, 1–9 (2021).

10. Edalati, P., Mohammadi, A., Ketabchi, M. & Edalati, K. Microstructure and microhardness of dual-phase high-entropy alloy by high-pressure torsion: Twins and stacking faults in FCC and dislocations in BCC. *J Alloys Compd* **894**, (2022).

11. Li, Z., Pradeep, K. G., Deng, Y., Raabe, D. & Tasan, C. C. Metastable high-entropy dual-phase alloys overcome the strength-ductility trade-off. *Nature* **534**, 227–230 (2016).

12. Jung, Y. *et al.* Investigation of phase-transformation path in TiZrHf(VNbTa)x refractory high-entropy alloys and its effect on mechanical property. *J Alloys Compd* **886**, 161187 (2021).

13. Yeh, J. W. Recent progress in high-entropy alloys. *Annales de Chimie: Science des Materiaux* **31**, 633–648 (2006).

14. Takeuchi, A. & Inoue, A. Mixing enthalpy of liquid phase calculated by miedema's scheme and approximated with sub-regular solution model for assessing forming ability of amorphous and glassy alloys. *Intermetallics (Barking)* **18**, 1779–1789 (2010).

15. Miracle, D. B. *et al.* Exploration and development of high entropy alloys for structural applications. *Entropy* **16**, 494–525 (2014).

16. Hsu, C., Yeh, J., Chen, S. & Shun, T. Wear Resistance and High-Temperature Compression Strength of Fcc CuCoNiCrAl ^ s ... *Metallurgical and Material Transcations A* **35A**, 1465–1469 (2004).

17. Yeh, J.-W. *et al.* Formation of simple crystal structures in Cu-Co-Ni-Cr-Al-Fe-Ti-V alloys with multiprincipal metallic elements. *Metallurgical and Materials Transactions A* **35**, 2533–2536 (2004).

18. Tsai, K. Y., Tsai, M. H. & Yeh, J. W. Sluggish diffusion in Co-Cr-Fe-Mn-Ni high-entropy alloys. *Acta Mater* **61**, 4887–4897 (2013).

19. Yeh, J. W., Chang, S. Y., Hong, Y. Der, Chen, S. K. & Lin, S. J. Anomalous decrease in X-ray diffraction intensities of Cu-Ni-Al-Co-Cr-Fe-Si alloy systems with multi-principal elements. *Mater Chem Phys* **103**, 41–46 (2007).

20. Zhang, Y., Zhou, Y. J., Lin, J. P., Chen, G. L. & Liaw, P. K. Solid-solution phase formation rules for multi-component alloys. *Adv Eng Mater* **10**, 534–538 (2008).

21. Murty, B. S., Yeh, J. W., Ranganathan, S. & Bhattacharjee, P. P. *High-entropy alloys, 2nd edition*. *Elsevier* (2019).

22. Tsai, M. H., Yeh, J. W. & Gan, J. Y. Diffusion barrier properties of AlMoNbSiTaTiVZr high-entropy alloy layer between copper and silicon. *Thin Solid Films* **516**, 5527–5530 (2008).

23. Tong, C. J. *et al.* Microstructure characterization of AlxCoCrCuFeNi high-entropy alloy system with multiprincipal elements. *Metall Mater Trans A Phys Metall Mater Sci* **36**, 881–893 (2005).

24. Ng, C., Guo, S., Luan, J., Shi, S. & Liu, C. T. Entropy-driven phase stability and slow diffusion kinetics in an Al 0.5CoCrCuFeNi high entropy alloy. *Intermetallics (Barking)* **31**, 165–172 (2012).

25. Chang, H. W. *et al.* Influence of substrate bias, deposition temperature and post-deposition annealing on the structure and properties of multi-principal-component (AlCrMoSiTi)N coatings. *Surf Coat Technol* **202**, 3360–3366 (2008).

26. Ranganathan, S. *Alloyed pleasures: Multimetallic cocktails*. *CURRENT SCIENCE* vol. 85 (2003).

27. Jiang, H. *et al.* Effect of Niobium on Microstructure and Properties of the CoCrFeNbxNi High Entropy Alloys. *J Mater Sci Technol* **33**, 712–717 (2017).

28. Müller, F. *et al.* On the oxidation mechanism of refractory high entropy alloys. *Corros Sci* **159**, (2019).

29. Butler, T. M. & Chaput, K. J. Native oxidation resistance of Al20Nb30Ta10Ti30Zr10 refractory complex concentrated alloy (RCCA). *J Alloys Compd* **787**, 606–617 (2019).

30. Wei, S. *et al.* Natural-mixing guided design of refractory high-entropy alloys with as-cast tensile ductility. *Nat Mater* **19**, 1175–1181 (2020).

31. Guo, S. & Liu, C. T. Phase stability in high entropy alloys: Formation of solid-solution phase or amorphous phase. *Progress in Natural Science: Materials International* **21**, 433–446 (2011).

32. Guo, S., Ng, C., Lu, J. & Liu, C. T. Effect of valence electron concentration on stability of fcc or bcc phase in high entropy alloys. *J Appl Phys* **109**, (2011).

33. Spencer, P. J. A brief history of CALPHAD. *CALPHAD* **32**, 1–8 (2008).

34. Gorsse, S. & Senkov, O. N. About the reliability of CALPHAD predictions in multicomponent systems. *Entropy* **20**, 1–9 (2018).

35. Kaufman, L. & Ågren, J. CALPHAD, first and second generation - Birth of the materials genome. *Scr Mater* **70**, 3–6 (2014).

36. Senkov, O. N., Miracle, D. B., Chaput, K. J. & Couzinie, J. P. Development and exploration of refractory high entropy alloys - A review. *J Mater Res* **33**, 3092–3128 (2018).

37. Raman, L. *et al.* Strengthening mechanisms in CrMoNbTiW refractory high entropy alloy. *Materials Science and Engineering: A* **819**, 141503 (2021).

38. Liu, C. M., Wang, H. M., Zhang, S. Q., Tang, H. B. & Zhang, A. L. Microstructure and oxidation behavior of new refractory high entropy alloys. *J Alloys Compd* **583**, 162–169 (2014).

39. El-Atwani, O. *et al.* Outstanding radiation resistance of tungsten-based high-entropy alloys. *Sci Adv* **5**, 1–10 (2019).

40. El Atwani, O. *et al.* A quinary WTaCrVHf nanocrystalline refractory high-entropy alloy withholding extreme irradiation environments. *Nat Commun* **14**, 1–12 (2023).

41. Yao, H. W. *et al.* Mechanical properties of refractory high-entropy alloys: Experiments and modeling. *J Alloys Compd* **696**, 1139–1150 (2017).

42. Senkov, O. N., Woodward, C. & Miracle, D. B. Microstructure and Properties of Aluminum-Containing Refractory High-Entropy Alloys. *JOM* **66**, 2030–2042 (2014).

43. Senkov, O. N., Senkova, S. V., Miracle, D. B. & Woodward, C. Mechanical properties of low-density, refractory multi-principal element alloys of the Cr-Nb-Ti-V-Zr system. *Materials Science and Engineering A* **565**, 51–62 (2013).

44. Senkov, O. N., Senkova, S. V, Woodward, C. & Miracle, D. B. Low-density, refractory multi-principal element alloys of the Cr–Nb–Ti–V–Zr system: Microstructure and phase analysis. *Acta Mater* **61**, 1545–1557 (2013).

45. Feng, R. *et al.* Superior High-Temperature Strength in a Supersaturated Refractory High-Entropy Alloy. *Advanced Materials* **33**, 1–9 (2021).

46. Stepanov, N. D., Shaysultanov, D. G., Salishchev, G. A. & Tikhonovsky, M. A. Structure and mechanical properties of a light-weight AlNbTiV high entropy alloy. *Mater Lett* **142**, 153–155 (2015).

47. Senkov, O. N., Senkova, S. V. & Woodward, C. Effect of aluminum on the microstructure and properties of two refractory high-entropy alloys. *Acta Mater* **68**, 214–228 (2014).

48. Senkov, O. N. *et al.* Microstructure and elevated temperature properties of a refractory TaNbHfZrTi alloy. *J Mater Sci* **47**, 4062–4074 (2012).

49. Guo, N. N. *et al.* Microstructure and mechanical properties of refractory MoNbHfZrTi high-entropy alloy. *Materials and Design* vol. 81 87–94 Preprint at https://doi.org/10.1016/j.matdes.2015.05.019 (2015).

50. Liu, S., Gao, M. C., Liaw, P. K. & Zhang, Y. Microstructures and mechanical properties of AlxCrFeNiTi0.25alloys. *J Alloys Compd* **619**, 610–615 (2015).

51. Sheikh, S. *et al.* Alloy design for intrinsically ductile refractory high-entropy alloys. *J Appl Phys* **120**, (2016).

52. Soni, V., Senkov, O. N., Gwalani, B., Miracle, D. B. & Banerjee, R. Microstructural Design for Improving Ductility of An Initially Brittle Refractory High Entropy Alloy. *Sci Rep* **8**, 8816 (2018).

53. Wan, Y. *et al.* Mechanical Properties and Phase Stability of WTaMoNbTi Refractory High-Entropy Alloy at Elevated Temperatures. *Acta Metallurgica Sinica (English Letters)* **34**, 1585–1590 (2021).

54. Alvi, S., Waseem, O. A. & Akhtar, F. High Temperature Performance of Spark Plasma Sintered W0.5(TaTiVCr)0.5 Alloy. *Metals (Basel)* **10**, 1512 (2020).

55. Soni, V. *et al.* Phase stability and microstructure evolution in a ductile refractory high entropy alloy Al10Nb15Ta5Ti30Zr40. *Materialia (Oxf)* **9**, 100569 (2020).

56. Lederer, Y., Toher, C., Vecchio, K. S. & Curtarolo, S. The search for high entropy alloys: A high-throughput ab-initio approach. *Acta Mater* **159**, 364–383 (2018).

57. Huang, H. *et al.* On cooling rates dependence of microstructure and mechanical properties of refractory high-entropy alloys HfTaTiZr and HfNbTiZr. *Scripta Materialia* vol. 211 Preprint at https://doi.org/10.1016/j.scriptamat.2022.114506 (2022).

58. Iroc, L. K. *et al.* Design of oxygen-doped TiZrHfNbTa refractory high entropy alloys with enhanced strength and ductility. *Mater Des* **223**, (2022).

59. Ghadyani, M., Utton, C. & Tsakiropoulos, P. Microstructures and isothermal oxidation of the alumina scale forming Nb1.45Si2.7Ti2.25Al3.25Hf0.35 and Nb1.35Si2.3Ti2.3Al3.7Hf0.35 Alloys. *Materials* **12**, 1–26 (2019).

60. Waseem, O. A., Auyeskhan, U., Lee, H. M. & Ryu, H. J. A combinatorial approach for the synthesis and analysis of AlxCryMozNbTiZr high-entropy alloys: Oxidation behavior. *J Mater Res* **33**, 3226–3234 (2018).

61. Gorr, B. *et al.* A new strategy to intrinsically protect refractory metal based alloys at ultra high temperatures. *Corros Sci* **166**, (2020).

62. Lo, K. C., Chang, Y. J., Murakami, H., Yeh, J. W. & Yeh, A. C. An oxidation resistant refractory high entropy alloy protected by CrTaO 4 - based oxide. *Sci Rep* **9**, 3–4 (2019).

63. Yurchenko, N., Panina, E., Zherebtsov, S., Salishchev, G. & Stepanov, N. Oxidation behavior of refractory AlNbTiVZr0.25 high-entropy alloy. *Materials* **11**, 1–15 (2018).

64. Gorr, B. *et al.* High-Temperature Oxidation Behavior of Refractory High-Entropy Alloys: Effect of Alloy Composition. *Oxidation of Metals* **88**, 339–349 (2017).

65. Gorr, B. *et al.* Current Status of Research on the Oxidation Behavior of Refractory High Entropy Alloys. *Advanced Engineering Materials* vol. 23 Preprint at https://doi.org/10.1002/adem.202001047 (2021).

66. Chang, C. H., Titus, M. S. & Yeh, J. W. Oxidation Behavior between 700 and 1300 °C of Refractory TiZrNbHfTa High-Entropy Alloys Containing Aluminum. *Adv Eng Mater* **20**, 1–8 (2018).

67. Pickering, E. J. *et al.* High-entropy alloys for advanced nuclear applications. *Entropy* **23**, 1–28 (2021).

68. Cheng, Z. *et al.* Irradiation effects in high-entropy alloys and their applications. *J Alloys Compd* **930**, 166768 (2023).

69. Egami, T., Guo, W., Rack, P. D. & Nagase, T. Irradiation resistance of multicomponent alloys. *Metall Mater Trans A Phys Metall Mater Sci* **45**, 180–183 (2014).

70. Xia, S. qin, Wang, Z., Yang, T. fei & Zhang, Y. Irradiation Behavior in High Entropy Alloys. *Journal of Iron and Steel Research International* **22**, 879–884 (2015).

71. Shi, T. *et al.* Current development of body-centered cubic high-entropy alloys for nuclear applications. *Tungsten* **3**, 197–217 (2021).

72. Li, T.-X. *et al.* Tungsten-containing high-entropy alloys: a focused review of manufacturing routes, phase selection, mechanical properties, and irradiation resistance properties. *Tungsten* **3**, 181–196 (2021).

73. Li, J., Fang, Q. & Liaw, P. K. Microstructures and Properties of High-Entropy Materials: Modeling, Simulation, and Experiments. *Adv Eng Mater* **23**, 1–30 (2021).

74. Waseem, O. A., Woller, K. B., Sweidan, F. B. & Ryu, H. J. Effects of F3+ ion implantation on the properties of W and W0.5(TaTiVCr)0.5 for depth marker-based plasma erosion analysis. *Nuclear Materials and Energy* **25**, 100806 (2020).

75. Sadeghilaridjani, M. *et al.* Ion irradiation response and mechanical behavior of reduced activity high entropy alloy. *Journal of Nuclear Materials* **529**, 151955 (2020).

76. Patel, D. *et al.* Radiation damage tolerance of a novel metastable refractory high entropy alloy V2.5Cr1.2WMoCo0.04. *Journal of Nuclear Materials* **531**, 152005 (2020).

77. Chen, Y. Y., Duval, T., Hung, U. D., Yeh, J. W. & Shih, H. C. Microstructure and electrochemical properties of high entropy alloys-a comparison with type-304 stainless steel. *Corros Sci* **47**, 2257–2279 (2005).

78. Zhang, Y. *et al.* Microstructures and properties of high-entropy alloys. *Prog Mater Sci* **61**, 1–93 (2014).

79. Bashev, V. F. & Kushnerov, O. I. Structure and properties of cast and splat-quenched high-entropy Al–Cu–Fe–Ni–Si alloys. *Physics of Metals and Metallography* **118**, 39–47 (2017).

80. Das, S. & Robi, P. S. Mechanical Alloying of W-Mo-V-Cr-Ta High Entropy Alloys. *IOP Conf Ser Mater Sci Eng* **346**, (2018).

81. Zhang, A., Han, J., Meng, J., Su, B. & Li, P. Rapid preparation of AlCoCrFeNi high entropy alloy by spark plasma sintering from elemental powder mixture. *Mater Lett* **181**, 82–85 (2016).

82. Ajay Kumar, P. & Perugu, C. S. Synthesis of FeCrVNbMn High Entropy Alloy by Mechanical Alloying and Study of their Microstructure and Mechanical Properties BT - TMS 2018 147th Annual Meeting & Exhibition Supplemental Proceedings. in (ed. & Materials Society Metals, T. M.) 669–675 (Springer International Publishing, 2018).

83. Pan, J. *et al.* Microstructure and mechanical properties of Nb25Mo25Ta25W25 and Ti8Nb23Mo23Ta23W23 high entropy alloys prepared by mechanical alloying and spark plasma sintering. *Materials Science and Engineering: A* **738**, 362–366 (2018).

84. Yan, J. H., Li, M. J., Li, K., Qiu, J. W. & Guo, Y. Effects of Cr Content on Microstructure and Mechanical Properties of WMoNbTiCr High-Entropy Alloys. *J Mater Eng Perform* **29**, 2125–2133 (2020).

85. Herzog, D., Seyda, V., Wycisk, E. & Emmelmann, C. Additive manufacturing of metals. *Acta Mater* **117**, 371–392 (2016).

86. Opprecht, M., Garandet, J. P., Roux, G., Flament, C. & Soulier, M. A solution to the hot cracking problem for aluminium alloys manufactured by laser beam melting. *Acta Mater* **197**, 40–53 (2020).

87. Piglione, A. *et al.* Printability and microstructure of the CoCrFeMnNi high-entropy alloy fabricated by laser powder bed fusion. *Mater Lett* **224**, 22–25 (2018).

88. Torralba, J. M., Alvaredo, P. & García-Junceda, A. High-entropy alloys fabricated via powder metallurgy. A critical review. *Powder Metallurgy* **62**, 84–114 (2019).

89. Jiao, L. *et al.* Femtosecond laser produced hydrophobic hierarchical structures on additive manufacturing parts. *Nanomaterials* **8**, (2018).

90. Knoll, H. *et al.* Combinatorial Alloy Design by Laser Additive Manufacturing. *Steel Res Int* **88**, 1–11 (2017).

91. Chen, S., Tong, Y. & Liaw, P. K. Additive manufacturing of high-entropy alloys: A review. *Entropy* **20**, (2018).

92. Dobbelstein, H., Thiele, M., Gurevich, E. L., George, E. P. & Ostendorf, A. Direct metal deposition of refractory high entropy alloy MoNbTaW. *Phys Procedia* **83**, 624–633 (2016).

93. Wang, R., Zhang, K., Davies, C. & Wu, X. Evolution of microstructure, mechanical and corrosion properties of AlCoCrFeNi high-entropy alloy prepared by direct laser fabrication. *J Alloys Compd* **694**, 971–981 (2017).

94. Dobbelstein, H., Gurevich, E. L., George, E. P., Ostendorf, A. & Laplanche, G. Laser metal deposition of compositionally graded TiZrNbTa refractory high-entropy alloys using elemental powder blends. *Addit Manuf* **25**, 252–262 (2019).

95. Dobbelstein, H. *et al.* Laser metal deposition of refractory high-entropy alloys for high-throughput synthesis and structure-property characterization. *International Journal of Extreme Manufacturing* **3**, (2020).

96. Lee, J. *et al.* Review on quality control methods in metal additive manufacturing. *Applied Sciences (Switzerland)* **11**, 1–16 (2021).

97. Svetlizky, D. *et al.* The influence of laser directed energy deposition (DED) processing parameters for Al5083 studied by central composite design. *Journal of Materials Research and Technology* **17**, 3157–3171 (2022).

98. Dass, A. & Moridi, A. State of the art in directed energy deposition: From additive manufacturing to materials design. *Coatings* **9**, 1–26 (2019).

99. Svetlizky, D. *et al.* Directed energy deposition (DED) additive manufacturing: Physical characteristics, defects, challenges and applications. *Materials Today* **49**, 271–295 (2021).

100. Haley, J. C. *et al.* Working distance passive stability in laser directed energy deposition additive manufacturing. *Mater Des* **161**, 86–94 (2019).

101. De˛bski, A., De˛bski, R. & Gasior, W. New features of Entall database: Comparison of experimental and model formation enthalpies. *Archives of Metallurgy and Materials* **59**, 1337–1343 (2014).

102. Senkov, O. N., Senkova, S. V., Woodward, C. & Miracle, D. B. Low-density, refractory multi-principal element alloys of the Cr-Nb-Ti-V-Zr system: Microstructure and phase analysis. *Acta Mater* **61**, 1545–1557 (2013).

103. Yao, H. W. *et al.* NbTaV-(Ti,W) refractory high-entropy alloys: Experiments and modeling. *Materials Science and Engineering A* **674**, 203–211 (2016).

104. Thermo-Calc Software. TCS High Entropy Alloys Database (TCHEA5). (2021).

105. Chen, B., Li, X., Chen, W., Shang, L. & Jia, L. Microstructural evolution, mechanical and wear properties, and corrosion resistance of as-cast CrFeNbTiMox Refractory high entropy alloys. *Intermetallics (Barking)* **155**, 107829 (2023).

106. George, E. P., Curtin, W. A. & Tasan, C. C. High entropy alloys: A focused review of mechanical properties and deformation mechanisms. *Acta Mater* **188**, 435–474 (2020).

107. Pacheco, V. *et al.* Thermal Stability of the HfNbTiVZr High-Entropy Alloy. *Inorg Chem* **58**, 811–820 (2019).

108. Tong, Z. *et al.* Laser additive manufacturing of FeCrCoMnNi high-entropy alloy: Effect of heat treatment on microstructure, residual stress and mechanical property. *J Alloys Compd* **785**, 1144–1159 (2019).

109. Tong, Z. *et al.* Microstructure, microhardness and residual stress of laser additive manufactured CoCrFeMnNi high-entropy alloy subjected to laser shock peening. *J Mater Process Technol* **285**, 116806 (2020).

110. Liu, F. *et al.* Microstructure and residual stress of laser rapid formed Inconel 718 nickel-base superalloy. *Opt Laser Technol* **43**, 208–213 (2011).

111. Attar, H., Calin, M., Zhang, L. C., Scudino, S. & Eckert, J. Manufacture by selective laser melting and mechanical behavior of commercially pure titanium. *Materials Science and Engineering A* **593**, 170–177 (2014).

112. Nguyen, V. T. *et al.* Cuboid-like nanostructure strengthened equiatomic Ti–Zr–Nb–Ta medium entropy alloy. *Materials Science and Engineering A* **798**, (2020).

113. Kunimine, T., Miyazaki, R., Yamashita, Y. & Funada, Y. Effects of Laser-Beam Defocus on Microstructural Features of Compositionally Graded WC/Co-Alloy Composites Additively Manufactured by Multi-Beam Laser Directed Energy Deposition. *Sci Rep* **10**, 1–11 (2020).

114. Sémoroz, A., Durandet, Y. & Rappaz, M. EBSD characterization of dendrite growth directions, texture and misorientations in hot-dipped Al-Zn-Si coatings. *Acta Mater* **49**, 529–541 (2001).

115. Zhang, W., Chabok, A., Kooi, B. J. & Pei, Y. Additive manufactured high entropy alloys: A review of the microstructure and properties. *Mater Des* **220**, 110875 (2022).

116. Gou, S. *et al.* Additive manufacturing of ductile refractory high-entropy alloys via phase engineering. *Acta Mater* **248**, 118781 (2023).

117. Tian, X. *et al.* Isotropic and improved tensile properties of Ti-6Al-4V achieved by in-situ rolling in direct energy deposition. *Addit Manuf* **46**, 102151 (2021).

118. Mills, K. C., Monaghan, B. J. & Keene, B. J. Thermal conductivity of molten metals: Part 1 Pure metals. Preprint at (1996).

119. Aydogan, E. *et al.* In-situ radiation response of additively manufactured modified Inconel 718 alloys. *Addit Manuf* **51**, (2022).

120. Yalcin, M. Y., Derin, C. B. & Aydogan, E. Development and Additive Manufacturing of Oxide Dispersion Strengthened Inconel 718: Thermochemical and Experimental Studies. *SSRN Electronic Journal* **914**, 165193 (2022).

121. Wang, R. *et al.* Achieving high strength and ductility in nitrogen-doped refractory high-entropy alloys. *Mater Des* **213**, (2022).

122. Wu, M. *et al.* Dislocation glide and mechanical twinning in a ductile VNbTi medium entropy alloy. *J Mater Sci Technol* **110**, 210–215 (2022).

123. Fischer, F. D., Svoboda, J., Appel, F. & Kozeschnik, E. Modeling of excess vacancy annihilation at different types of sinks. *Acta Mater* **59**, 3463–3472 (2011).

124. Jiang, S. *et al.* Interstitial carbon induced FCC-Ti exhibiting ultrahigh strength in a Ti37Nb28Mo28-C7 complex concentrated alloy. *Acta Mater* **203**, (2021).

125. Jing, R., Liu, C. Y., Ma, M. Z. & Liu, R. P. Microstructural evolution and formation mechanism of FCC titanium during heat treatment processing. *J Alloys Compd* **552**, 202–207 (2013).

126. Han, G. *et al.* Face-centered-cubic titanium - A new crystal structure of Ti in a Ti-8Mo-6Fe alloy. *J Alloys Compd* **748**, 943–952 (2018).

127. Wei, B., Ni, S., Liu, Y. & Song, M. Three dimensional crystallographic orientation relationships for hexagonal close packed structure to face centered cubic structure transformation in pure titanium. *Scr Mater* **169**, 46–51 (2019).

128. Wu, H. C. *et al.* Rolling-induced face centered cubic titanium in hexagonal close packed titanium at room temperature. *Sci Rep* **6**, 1–8 (2016).

129. Li, Z. *et al.* Strength-ductility synergy of Al-bearing low-density refractory TiNbMo0.5AlX medium entropy alloys via precipitation. *Materials Science and Engineering: A* **844**, (2022).

130. Chang, Y. *et al.* Could face-centered cubic titanium in cold-rolled commercially-pure titanium only be a Ti-hydride? *Scr Mater* **178**, 39–43 (2020).

131. Xiong, T. *et al.* Faceted Kurdjumov-Sachs interface-induced slip continuity in the eutectic high-entropy alloy, AlCoCrFeNi2.1. *J Mater Sci Technol* **65**, 216–227 (2021).

132. Ma, E. Instabilities and ductility of nanocrystalline and ultrafine-grained metals. *Scr Mater* **49**, 663–668 (2003).

133. Du, X. H. *et al.* Dual heterogeneous structures lead to ultrahigh strength and uniform ductility in a Co-Cr-Ni medium-entropy alloy. *Nat Commun* **11**, 1–7 (2020).

134. Xia, M. *et al.* Synthesis of WTaMoNbZr refractory high-entropy alloy powder by plasma spheroidization process for additive manufacturing. *J Alloys Compd* **917**, 165501 (2022).

135. Zhang, D. L. & Ying, D. Y. Formation of fcc titanium during heating high energy ball milled Al-Ti powders. *Mater Lett* **52**, 329–333 (2002).

136. Huhn, W. P. & Widom, M. Prediction of A2 to B2 phase transition in the high-entropy alloy Mo-Nb-Ta-W. *Jom* **65**, 1772–1779 (2013).

137. Wang, F. *et al.* Effect of Mo on the morphology, microstructure and mechanical properties of NbTa0.5TiMox refractory high entropy alloy fabricated by laser powder bed fusion using elemental mixed powders. *Int J Refract Metals Hard Mater* **111**, 106107 (2023).

138. Hu, Q., Guo, S., Guo, J. L., Luo, F. F. & Wang, J. W. Effect of Mo on high-temperature strength of refractory complex concentrated alloys: A perspective of electronegativity difference. *J Alloys Compd* **906**, (2022).